Edited by Gianfranco Pacchioni
and Sergio Valeri

WILEY-VCH

Oxide Ultrathin Films

Science and Technology

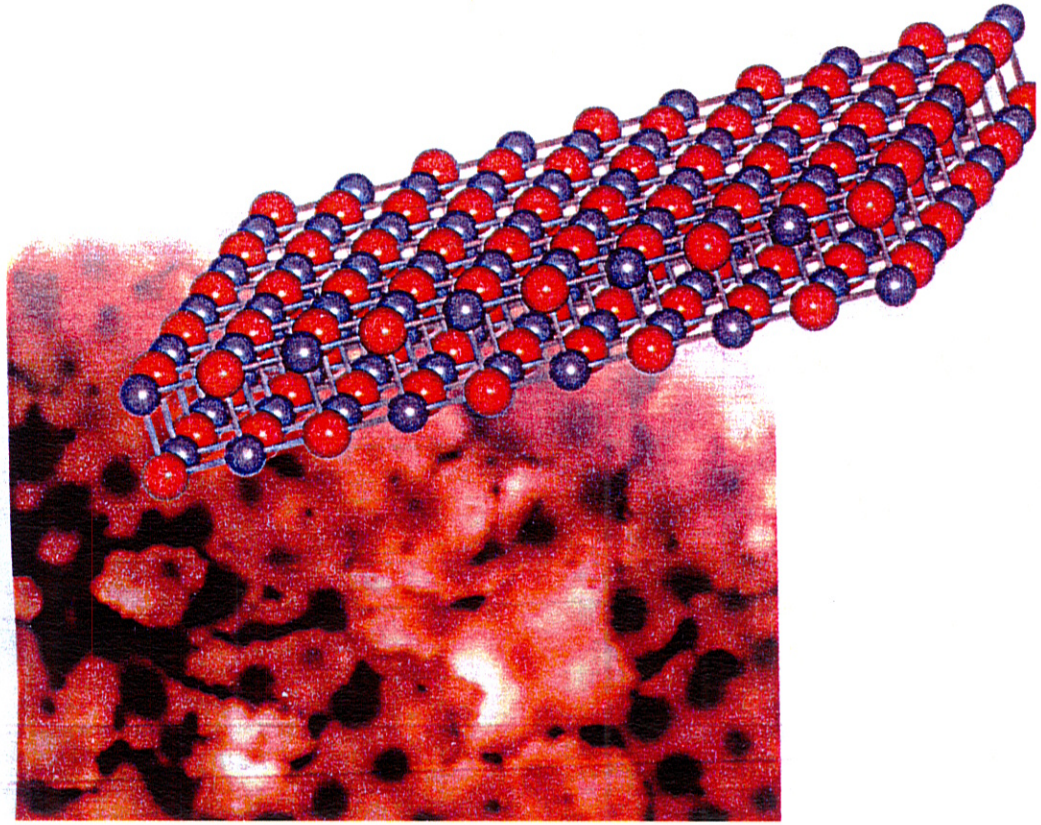

7

Oxide Films as Catalytic Materials and Models of Real Catalysts

Hans-Joachim Freund

7.1

Introduction

Unwilling to live with the experimental constraints that the insulating properties of oxide single crystals impose on the experimenter [1–4] when applying the tools developed in surface science to study elementary processes in catalysis on metal surfaces, a number of groups in the USA and Europe in the late 1980s started to investigate the possible use of thin oxide films as materials that could substitute for bulk oxides in model systems [5–16]. While amorphous silica films covering silicon surfaces when exposed to air had been used previously to model supports for metal nanoparticles [5, 17–27], the investigation of ordered films claimed at revealing the influence of the atomic detail of oxide surfaces on the interaction with adsorbates and metal particles [27–29]. This opened up by applying the rules of epitaxial growth to oxide films grown on metal and alloy surfaces. The strategy also opened the way to today's use of oxide films to study the phenomena that are covered in the various chapters of this book. The present chapter is dedicated to the use of oxide films to establish reliable models of heterogeneous catalysts that capture some of the complexity represented by technologically employed disperse metal catalysts and to the use of ultrathin films as potential catalysts in their own right.

Figure 7.1 shows a schematic of the kind of model systems studied. Such systems will be addressed in this chapter. There are two classes of model systems. The first, in which the goal is to represent a disperse supported metal or a mixed oxide catalyst, is shown on the left-hand side of Figure 7.1 and the model systems are based on the ability to model the bulk or volume of a supporting oxide using thin-film techniques. In the second class of model systems, shown on the right-hand side of Figure 7.1, the thickness of the oxide film and the oxide–metal interface created by growing the film are used as decisive parameters to control the electronic structure. This may influence either a supported deposit, for example a metal atom or nanoparticle, or the film itself, by the chemical potential of the gas phase, resulting in the formation of a catalytically active phase. The phenomena observed for this second class of materials are very much influenced by the

Oxide Ultrathin Films: Science and Technology, First Edition.
Edited by Gianfranco Pacchioni and Sergio Valeri.
© 2012 WILEY-VCH Verlag GmbH & Co. KGaA, Weinheim.
Published 2012 by WILEY-VCH Verlag GmbH & Co. KGaA

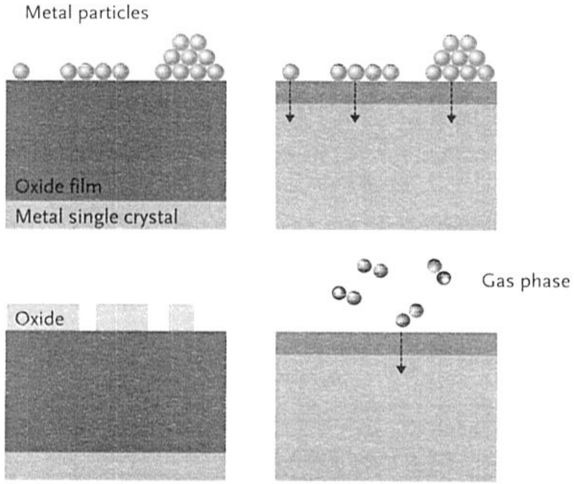

Figure 7.1 Schematic of classes of model systems [30].

flexibility that the oxide lattice of a thin film exhibits as compared to the bulk material, and may provide a new route to catalyst design.

Section 7.2 documents the control of epitaxial growth and points out implications for studies with adsorbates and deposited particles of active components, either metal or another oxide. Section 7.3 deals with case studies, that is, with gold nanoparticles and their charge state exhibiting potential influence on catalysis by gold, and with vanadia particles on ceria active in methanol oxidation. Section 7.4 addresses another very interesting aspect of ultrathin films, that is, their inherent activity as indicated above. We concentrate on ultrathin magnesia and alumina films with metal deposits on them, and finally, on the reactivity of ultrathin iron oxide films at elevated pressure.

7.2
Oxide Thin Films Grown as Supports

There have been a number of reviews on oxide film growth published over the years [6–9, 12, 13, 16]. A relatively simple system that was used early on by the Goodman group was MgO(100) on Mo(100) [17–27]. The high melting point of the refractory metal was thought to be an important factor to enable thermal treatment of the system after deposition of magnesium metal in oxygen ambient. This may be one reason why this system has found widespread applications. The disadvantage of this system, however, is the relatively large misfit between the lattice constants of MgO and molybdenum which is 5.3%. Figure 7.2 shows a series of scanning tunneling microscopy (STM) images taken as a function of thickness of the MgO layer [31]. At first uniform islands of MgO form on the Mo (100) surface with the open space between the islands exhibiting a (1×1) low-energy electron diffraction (LEED) pattern. Figure 7.2 also shows a schematic of the growth mode. Upon deposition of more MgO material an ordered network of misfit dislocations develops as we reach the equivalent of 2–4 deposited layers concomitant with the development of satellite spots in the LEED pattern as indicated in the inset. When the thickness is increased further, STM indicates the formation of screw dislocations and a pronounced mosaic spread which is also reflected in the LEED pattern. After even larger amounts of material have been deposited the layer relaxes the lattice constant to the bulk value and a broad single reflection is observed. The STM image shows a surface with flat terraces and steps to grain boundaries. These grain boundaries contain nonstoichiometric sites which could bind molecules from the gas phase or deposited metal atoms from a metal vapor to nucleate metal nanoparticles. However, there is yet another very drastic modification which is induced by the presence of the oxide film on a metallic substrate, that is, electron transfer from the metal into the grain boundaries as was pointed out in a theoretical study by Trevethan and Shluger [32]. Due to the nonstoichiometry, the work function of the grain boundaries differs from that of the flat terraces, and the concomitant potential difference may lead to the trapping of electrons from the metal substrate. This represents a phenomenon that is not directly connected with the properties of bulk MgO, neither single crystal nor powder, but rather with the specific oxide–metal interface, and it therefore cannot be used to explain the activity of working powder catalysts.

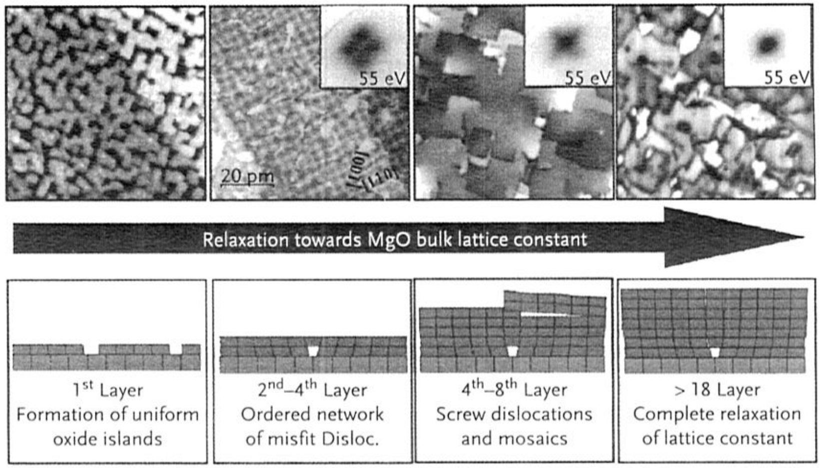

Figure 7.2 STM images of MgO (100)/Mo(001) as a function of deposited material. The lower panels show a schematic representation of the growth mode [31].

In the following we will provide evidence that the outlined scenario is operative for MgO films on Mo(100).

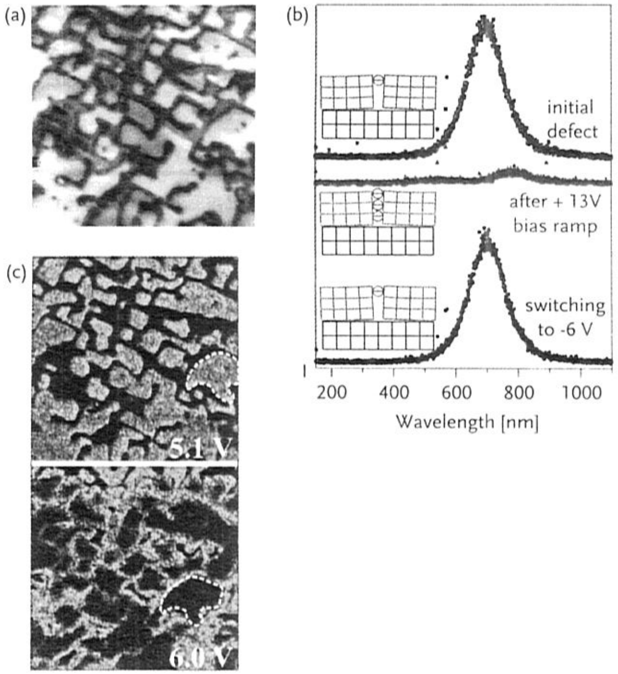

Figure 7.3 (a) High-bias series showing line defects as deep grooves in an oxide surface (0.05 nA and $100 \times 100\,\text{nm}^2$). (b) Light-emission spectra obtained from a pristine line defect (top) after a bias ramp to +13 V (center) and after reversing the polarity (bottom). All spectra acquired at +6 V sample bias and 1 nA current. The suppressed emission after the ramp is ascribed to electron trapping in the line defect, being reversed at negative bias (see insets). (c) Photon maps (1 nA and $75 \times 75\,\text{nm}^2$) taken at the bias position of the second FER on MgO terraces (top) and defect lines (bottom). The contrast reversal between both images reflects work function modulations in the film [33].

A first indication comes from a deviating electronic structure of the dislocation lines, as deduced from STM images obtained in the field-emission regime (Figures 7.2 and 7.3a). At high sample bias, the line defects are imaged with negative apparent height of up to −7 Å (Figure 7.3a) compared to the regular film, although the geometric corrugation deduced from low-bias images is below 2.5 Å (Figure 7.2).

The negative contrast indicates a low electron transmissibility of the line defects, forcing the tip to approach the surface in order to maintain a constant current. Electron transport at elevated bias is governed by field-emission resonances (FERs), which can be considered as vacuum states that develop in the classical part of a tip–sample junction [34]. Their energy is defined by the condition that multiples of half the free-electron wavelength fit into the triangular region confined by the tunnel barrier and the sample surface. Quantum mechanically, FERs are eigenstates E_n in a triangular potential, the bottom and slope of which are given by the sample work function Φ and the tip electric field F, respectively [35]:

$$E_n = \Phi + \left(\frac{3\pi h e \cdot F}{2\sqrt{2m}}\right)^{2/3} n^{2/3} \tag{7.1}$$

As FERs carry most of the tunnel current at high bias, their availability above the MgO surface determines the image contrast in STM. Apparently, the defect lines offer no FERs or fewer FERs than the regular oxide patches and consequently appear dark (Figure 7.2). According to Eq. (7.1), the energy position of the FER is primarily fixed by Φ, because the tip electric field is roughly constant in the feedback-controlled imaging mode employed here. The negative contrast therefore suggests a work function increase around the dislocation lines that moves the FER to higher energies. On defect-free oxide patches, the first and second FERs are reached around 3.7 and 5.4 V, respectively, with the exact value depending on the terrace size. Above the line defects, the first and second resonances are systematically up-shifted to about 4.4 and about 6.0 V, corroborating the local increase of the work function. Complementary information is obtained from STM light-emission spectra obtained from the MgO/Mo films. The experimental setup has been recently described [36]. Here the light emitted from a tunneling function between the tip and the sample is collected by a parabolic screen and imaged onto a CCD camera. As discussed in earlier work [37, 38], the optical response is governed by radiative electron transitions from higher to lower FER. The dominant peak at 1.75 eV (700 nm; Figure 7.3b) corresponds to a decay from the second to the first FER, while a weak shoulder at 2.5 eV (500 nm) involves the third and first FERs. The high cross section of the emission is because of the large tunnel barrier through the oxide film that gives rise to a long residence time for electrons in the FERs. Similar to the resonance states, the photon response is sensitive to the oxide work function as well. On regular MgO terraces, the emission becomes detectable between 4.8 and 5.5 V excitation bias, which covers the energy window of the second FER in this region. In contrast, no emission is observed below 5.8 V for the line defects, in agreement with an up-shift of the FER. The energy of the emission peak remains constant in both cases, reflecting the rigid shift of the FER with Φ. This bias difference can be exploited to display the work function distribution in the MgO film by mapping the integral photon yield as a function of sample bias (Figure 7.3c). In photon maps obtained at 5.1 V, only the flat MgO terraces with low Φ emit light and the defects remain dark. The contrast reverses at 6.0 V, as the optical channel opens in the defect regions.

Both electronic and optical spectroscopies conclusively reveal a work function increase of about 0.7 eV along MgO/Mo line defects with respect to the regular film. To explain this observation one needs to consider that oxide films in general modify the work function of a metal support. According to density functional theory (DFT) and Kelvin probe studies, the MgO film reduces Φ by about 1.5 eV [39–41]. The effect is caused by an electron transfer out of the film that creates a positive interface dipole, and the suppressed electron spill-out at the metal surface.

Surface defects may alter this trend due to their influence on the local charge distribution. While electron-poor defects, such as F^{2+} centers or cationic edge and corner sites produce positive surface dipoles that reduce Φ, electron-rich defects increase the charge density at the surface and hence the work function. The higher Φ value measured along MgO line defects is therefore compatible with a charge accumulation and indicates electron trapping in the dislocation lines. This conclusion is in agreement with DFT calculations that identified electrostatic pockets in the Madelung potential along an MgO grain boundary that can be filled with electrons [42]. The associated gap states are localized close to the conduction band onset. Due to the high energy of the electrostatic traps, electron trapping will be restricted to oxide films that are sufficiently thick to inhibit electron tunneling into the metal support.

Filling of the electrostatic traps in thicker films was achieved locally with STM (schematically indicated in Figure 7.3c). For this purpose, voltage ramps with enabled feedback loops were applied to the STM junction. The effect of electron trapping was then monitored by reversible changes in the optical response. As discussed above, a pristine defect emits photons at an excitation bias of 6.0 V. After ramping the bias to +13 V and returning to the initial situation, the photon signal vanishes (Figure 7.3) and recovers only after a quick reversal of the bias polarity. Apparently, electrons from the MgO valence band are excited into the shallow trap states at high bias, although those states are not directly accessible for tunneling due to their negligible overlap with the molybdenum wave functions. The trapped charges trigger a work function increase that renders the second FER unavailable for optical transitions with an excitation bias of 6.0 V. The electrons are only stabilized at positive bias, but leave the trap states at negative polarity most likely via tunneling to the tip. The subsequent discharging of the gap states restores the initial photon signal. A comparable hysteresis in the optical response is not observed on the oxide terraces, reflecting the crucial role of the line defects in the trapping phenomenon.

It is possible that trapped electrons in an oxide film could influence the charge state of adsorbed molecules and deposited metal particles and an example is further discussed below. The consequence is that one has to look for another metal substrate in order to circumvent the problem. Such a system was early on proposed by Wollschläger *et al.* [43, 44] and Valeri's group [45, 46]. They suggested preparing MgO on Ag(100) because the misfit is considerably smaller (2.9%). A detailed spot-profile analysis LEED study has been carried out for the defect structure of the MgO/Ag film and suggested a considerably smaller or even absent mosaic speed. This was basically corroborated by STM investigations by Schneider's group in Lausanne [47, 48] as well as by the group of the author [49–51]. Figure 7.4 shows STM images of an MgO(100) film on Ag(100) as the MgO coverage increases.

The film grows into a closed structure already starting from the first layer. Before the layer closes very small square islands with perfect epitaxy to the Ag(100) surface appear which coalesce into an almost perfect layer. A film of several layers is imaged exhibiting well-ordered terraces which may even be atomically resolved

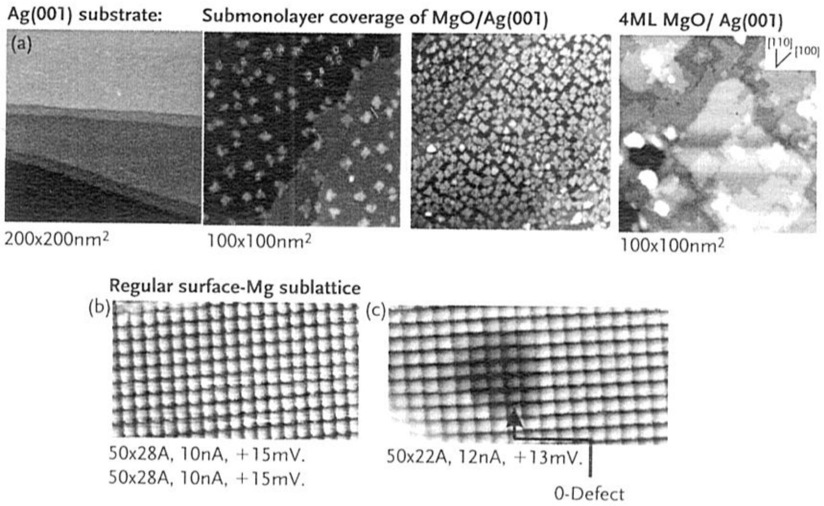

Figure 7.4 STM images of MgO(001)/Ag(001) for various MgO coverages: left top panel, clean surface; right top panel, fully covered surface. Atomically resolved STM image of (a) MgO(100) terrace, (b) pristine terrace, and (c) after electron bombardment (oxygen vacancy) (M. Sterrer, M. Heyde, and H.P. Rust, unpublished results).

(Figure 7.4b). There the tunneling conditions are such that the magnesium ions and their square arrangement are imaged, and the oxygen ions are invisible. Such a layered system does not show the granular morphology seen for MgO(100)/Mo(100). In order to create defects this film has to be bombarded with electrons in order to remove oxygen ions from the MgO lattice. The effect is shown in Figure 7.4b where the magnesium sublattice has been imaged in the presence of oxygen modifying the electronic structure of the surface to a separation of about two lattice constants away from the created defect.

Scanning tunneling spectroscopy (STS) and atomic force microscopy, in the form of frequency-modulated dynamic force microscopy (FM-DFM), can be used to study the detail of the electronic structure of those defects. Figure 7.5a shows at top left a topographic image of an MgO(100)/Ag(100) film and below an image in which oxygen defects at the terrace edges are visible. At top right an AFM image of F^{2+} defect is depicted. The F^0 and F^+ centers were produced by electron bombardment at room temperature, when the oxygen defects migrate from the terrace to the edges where they have lower formation energy due to the lower coordination at the step edge. Oxygen point defects in ionic materials are called color centers. The reason is that due to the missing O^{2-} ion the surrounding Mg^{2+} ions create a potential well that may trap one or two electrons. The color comes about because the electrons in the potential well develop quantum states like a particle in a box and the excitation of the electrons among the quantum states leads to a coloring of oxide single crystals when created in the bulk. A color center with no electrons is called an F^{2+}center, with one electron an F^+ center, and with two electrons an F^0

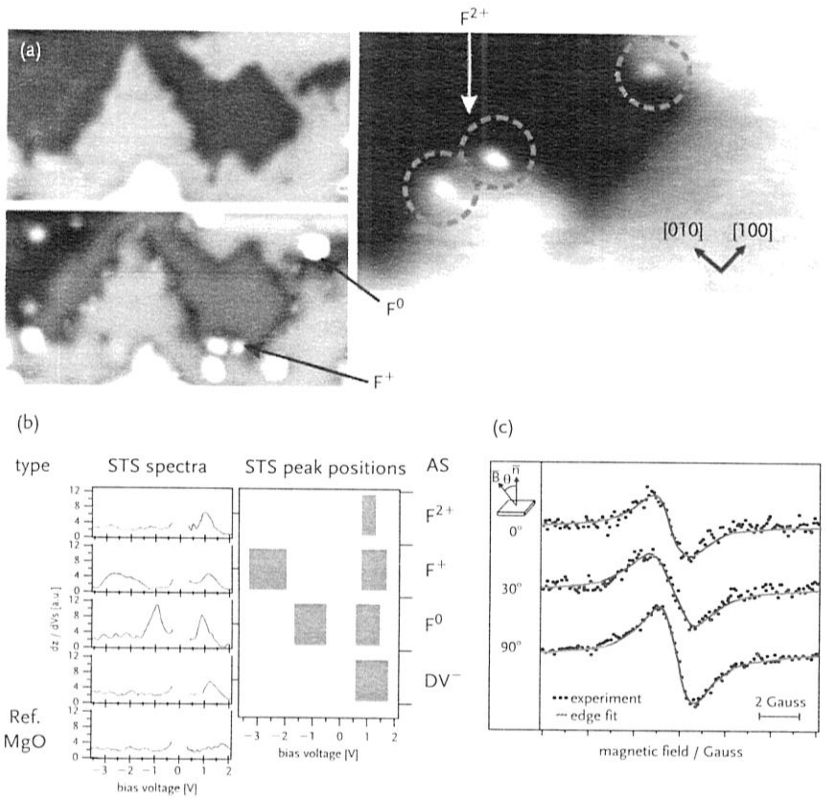

Figure 7.5 (a) Low-temperature (4 K) STM image ($28 \times 16\,nm^2$) of 4 ML thick MgO(001)/Ag (001) after electron bombardment at U bias $= +3.5$ V showing the morphology of the MgO film (top left), and at U bias $= -2.5$ V (bottom left) showing electronic surface defects. FM-DFM image (right) taken at constant Δf showing an MgO step edge with point defects (indicated by the dashed circles). Scan range: $23.0 \times 11.5\,nm^2$; $\Delta f = -1.6$ Hz; VS $= -50$ mV. (b) The right labels indicate the different defect types. The left graph shows STS spectra of the respective defect. The right graph presents the maxima of the STS data. The covered abscissa range accounts for the statistics of the peak positions. The relative shift of the local potential $\Delta\Phi_{rel}$ with respect to the MgO surface (bottom abscissa) and the absolute shift $\Delta\Phi_{abs}$ with respect to the Ag(001) level (top abscissa), both shifts including the local charge. (c) Experimental and simulated electron paramagnetic resoance spectra of color centers on a 20 ML thick MgO(001)/MoG(001). F^{2+}, doubly charged color center; F^+, singly charged color center; F^0, nutria color center; DV, divacancy [30, 41, 49, 52, 53].

center, where the superscript counts the number of uncompensated charges. In Figure 7.5b spectroscopic information on four different types of defects derived from STS and FM-DFM is collected. The assignment is based on results of calculations modeling the various defects, that is, F^{2+}, F^+, F^0, and an Mg–O di-vacancy. The lowermost STS trace refers to the reference which is undistorted MgO on Ag(100). Such information is important to identify the features observed in images such as the one shown in Figure 7.5a. In the case of F^+ centers, one may also prove their existence via electron spin resonance spectroscopy [49]. Those electron paramagnetic resonance investigations on single-crystal surfaces also allow one to determine the symmetry of the site from angle-dependent measurements of the g-tensor components (Figure 7.5c). The results are in full agreement with the conclusions drawn from the STM data.

In some cases there is an interesting variant of epitaxial growth: strain-induced formation of mixed oxide films at the oxide–metal interface. One such case has been observed for the growth of CaO(100) on Mo(100) [54, 55]. CaO is isostructural to MgO but differs in the misfit (8.3%) of the lattice constant. While MgO grows as a binary oxide with the expectation of a high density of defects as discussed in detail above, CaO(100) grows essentially defect free as the misfit strain is compensated by molybdenum incorporation within the film at the interface. The ternary Ca/Mo/O phase only forms as long as molybdenum is supplied from the metal reservoir below, but transforms into plain CaO above a critical thickness.

In some cases the mismatch can lead to self-limiting growth, as was found for FeO which crystallizes as a defect-rich rock salt bulk structure [56]. On a Pt(111) surface FeO grows as a perfect double layer with a pronounced Moiré pattern. The schematic structure shows that only with a large unit cell may a coincidence lattice be formed. Its structure has been well characterized and the structural parameters have been determined.

Cerium oxide has attracted interest in recent years as an active redox support material. CeO_2 films in (111) orientation may be grown on an Ru(0001) surface [58, 59]. Since CeO_2 has the CaF_2 structure the film grows in integers of triple (O–Ce–O) layers. Figure 7.6 shows STM images of the $CeO_2(111)$ surface of a film consisting of three triple layers. The film shows large terraces with a hexagonal arrangement of atomic protrusions which turn out to be due to tunneling into the empty Ce^{4+} states in the second layer below the terminating oxygen triangles. The surface also exhibits point defects. These defects have particular shapes which are caused by the reduction of $2Ce^{4+}$ centers due to the removal of an oxygen atom and the transfer of two electrons to Ce^{4+} ions in the neighborhood. Sauer's group has shown via density functional calculations [61] that the most stable configuration is not the expected one where the closest Ce^{4+} ions are reduced but rather a configuration where at least one cerium ion is somewhat removed from the proton of the removed oxygen. The resulting variation in the chemical environment leads to a splitting of the filled Ce^{3+} levels, which is detected with STS. The position of the Ce^{3+} ion pair is also reflected in a characteristic defect pattern observed in empty-state STM images, which results from the bright appearance of Ce^{4+} ions next to the defect while the Ce^{3+} ions remain dark. Both findings demonstrate that at least one extra electron localizes at a cerium ion that is not adjacent to the oxygen vacancy. This allows us to understand and interpret images when there are interactions of adparticles, as discussed below.

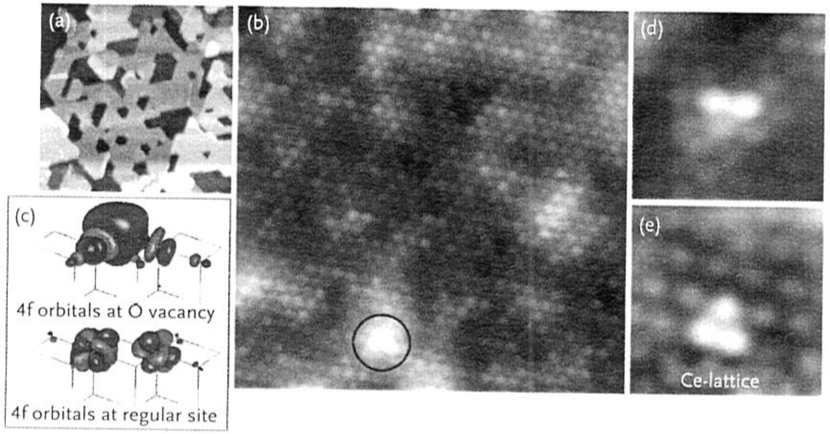

Figure 7.6 (a) STM image of a five trilayer thick CeO_2 film grown on Ru(0001) (3.1 V, 100 × 100 nm^2). (b) Atomically-resolved image showing the cerium sublattice (1.2 V, 12 × 12 nm^2). The protrusion in the lower part is assigned to a single oxygen vacancy. Similar defects imaged with a tip configuration that is sensitive to defects. (c) The origin of the contrast of the Ce^{4+} 4f orbitals in the presence of the vacancy as shown in (b). (d, e) Enlarged (2.4 × 2.4 nm^2) views of defect region. While two protrusions are observed at the defect site in (d), three emerge in (e) [60].

In addition, a number of oxide film systems, for example Al_3O_{12}/NiAl(110) [28], Cr_2O_3(111)/Cr(111) [62], Fe_2O_3(0001)/Pt(111) [63, 64], V_2O_3(0001)/Au(111) [65, 66], Fe_3O_4(111)/Pt(111) [67, 68], Nb_2O_5(111)/Cu_3Au(111) [69], and more, have been studied with respect to the use of model catalyst systems.

7.3
Systems to Model Real Catalysts

We discuss in the first example in this section the characterization of systems modeling supported dispersed metal catalysts with respect to the charge state of the active metal, and use supported gold as a prototype, because in this case the situation is perhaps most controversial. In the second case study we investigate the reactivity of supported oxide nanoparticles in the oxidation of methanol to formaldehyde.

7.3.1
Supported Gold

Catalysis by gold has become a topic of intense scientific study, probably because it was unexpected when Masatake Haruta on a sabbatical in Europe discovered that small gold particles catalyze CO oxidation at very low temperature. After this

discovery, a number of groups started to investigate the reasons for the activity. It is still controversial today. Is it a metal–insulator transition in the particle, a particular morphology, or the charge state of the particle that determines reactivity [70–76]? The situation is complicated by the fact that different charge states of gold may result from different preparation conditions (oxidative or reducing environment), the nature of the oxide support (reducible or non reducible), or the existence of defects on the support. In particular when thin oxide films were used, the conclusions drawn turned out to be strongly influenced by the chosen model system conditions. This is intimately connected with the points raised in Section 7.2 and will be discussed in detail using MgO films on molybdenum as an example in Section 7.4. It does not come as a surprise, therefore, that there is no single answer to the question: what is the charge state of a small gold cluster deposited on an oxide surface? Also the identification of the charge state of a gold nanoparticle is not trivial. Adsorption of CO "probe" molecules and the measurement of their vibrational properties are, together with analysis of binding energy shifts from X-ray photoelectron spectroscopic studies, often employed to identify the oxidation state of metal atoms or nanoparticles grown on oxide surfaces [77]. A CO frequency of about 2100–2120 cm^{-1} is typical of neutral gold particles or of the gold surface [78, 79]. Frequencies in the range 2130–2180 cm^{-1} correspond to the formation of gold clusters in a positive oxidation state [80], while for clusters with an accumulation of negative charge due, for instance, to the interaction with surface defects, the frequency is red-shifted and may vary considerably but is typically around 2040–2080 cm^{-1} [81–83]. The explanation of this trend is rather simple and is based on the classical Blyholder model [84], that is, the degree of population of the antibonding $2\pi^*$ orbital of CO via back-donation, which leads to a weakening of the bond and thus to a red shift of the CO stretching frequency. Analysis of the dependence of the CO frequency shift with respect to different Au—CO bonding contributions reveals a direct relationship between the CO stretching frequency and the amount of electronic charge back-donated from the metal to the CO $2\pi^*$ molecular orbital. In turn, this depends on the charge state of the metal, being largest for electron-rich species [85]. Exceptions to these "rules" do also exist. Recently, it has been shown that when CO interacts with a neutral gold atom deposited on an MgO surface its stretching frequency, instead of being close to that of the gas-phase molecule, is red-shifted by almost 300 cm^{-1} [86, 87]. This is due to an induced net charge transfer of one electron from the Au 6s valence orbital to the CO $2\pi^*$ molecular orbital, which occurs spontaneously upon CO adsorption, and is caused by the Pauli repulsion between the neutral gold atom's 6s electron and the closed-shell oxygen ion in the oxide surface, that is, the adsorption site of the gold atom. In this case the CO molecule does not probe the charge state of the as-deposited gold atom, but instead the strong chemical rearrangement following CO adsorption [86]. In the meantime, CO stretching frequencies between the limiting value for the gold atom and the range 2100–2120 cm^{-1} found for neutral gold aggregates have been observed for negatively charged gold atoms and clusters and neutral gold dimers and trimers [88].

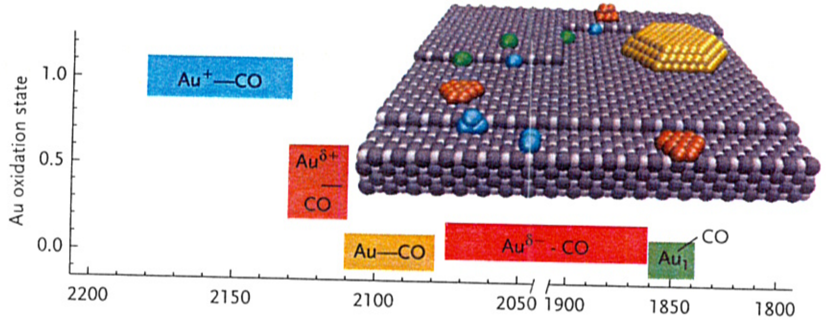

Figure 7.7 CO stretching frequency regions for CO adsorbed on gold nanoparticles [88].

Figure 7.7 illustrates the range of CO stretching frequencies observed so far for gold particles. Another important aspect in this matter is the perturbation of the electronic nature of the small metal aggregates that are formed on the surface by the interaction with the support. Charge transfer at the interface between the oxide and the metal cluster is not the only mechanism that determines the final shift in the CO frequency. CO is very sensitive to the details of the cluster electronic structure and, in particular, to the polarization of the metal electrons or the adsorption site; an increase in the Pauli repulsion between CO and the metal cluster can result in a blue shift of the frequency even in the absence of a positive charge. Furthermore, exposed cations and anions at the surface of ionic oxides generate local electric fields, which may interact with the CO multiple moments resulting in non-negligible shifts in the CO vibrational frequency. All these effects, charge transfer, electron polarization, adsorption site, Pauli repulsion, and local electric field, play an important role in supported metal clusters containing just a few atoms, while their effect is expected to rapidly vanish for particles containing tens or hundreds of atoms [85].

The big advantage of model studies is that those questions may now, for the first time, be addressed experimentally in detail because direct structure–spectroscopy relations may be established. Most of the experimental studies have been carried out with pristine oxide surfaces, devoid of any functional surface groups. However, in any realistic environment, the oxide termination is subject to changes according to the thermodynamic equilibrium imposed by the environment, and in almost all cases after exposure to air and at moderate temperature, an oxide will be covered by a certain amount of strongly bound hydroxyl groups. In order to bridge this materials gap, several groups reported on the selective modification of single-crystalline oxide surfaces with hydroxyl groups by exposure to water and investigated the properties of subsequently deposited metals [89–95]. The potential role of water and hydroxyl groups in catalysis over supported gold nanoparticles has been highlighted recently. As a co-reactant, small doses of water have been found to increase the catalytic activity in CO oxidation, which is partly attributed to activation of oxygen and to the transformation of tightly bound carbonate, which acts as a poison, into bicarbonate species that are able to release CO_2 at moderate temperature. Hydroxyl species on the oxide support represent strong anchoring sites for solution complexes during the preparation of gold catalysts by the deposition-precipitation method [96], and this interaction has been suggested to determine the final structure of supported gold nanoparticles [97]. The deposition of various amounts of gold on thick MgO(100) films prepared on Ag(100) that were either pristine or hydroxylated with water has been investigated as a function of temperature. The key techniques here are infrared spectroscopy, X-ray photoelectron spectroscopy, and STM. Figure 7.8a shows a set of Fourier transform infrared (FTIR) spectra in the stretching frequency region of CO obtained for 0.006 ML (trace second from top) and 0.02 ML (following traces) of gold deposited onto an MgO(100)/Ag(100) film with a thickness of 13 layers. The figure shows FTIR spectra taken at the given temperatures after exposure to saturation CO coverage at 90 K. The top trace is the spectrum of a hydroxylated (or rather deuteroxylated) MgO film surface for a gold coverage of 0.02 ML.

At the lowest coverage of 0.006 ML gold on pristine MgO(100), the main contribution to the spectrum obtained at 90 K is an absorption band centered at 2154 cm^{-1} exhibiting a shoulder at 2170 cm^{-1}. Two additional small signals appear at 2121 and 1850 cm^{-1}. As the coverage is increased to 0.02 ML gold all absorption bands increase in intensity. The band centered at 2170 cm^{-1} is now clearly resolved in this spectrum and the two absorption bands at 2154 and 2121 cm^{-1} are nearly equal in intensity. The bands observed at 2121 and 1850 cm^{-1} are well known for CO adsorbed on MgO(001)-supported gold atoms and clusters. A combined

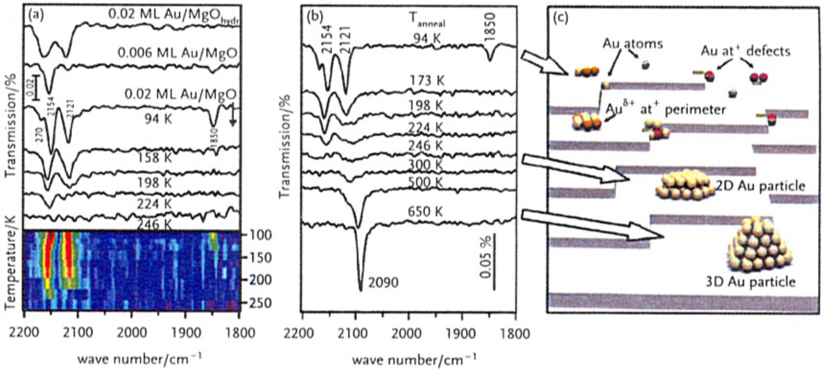

Figure 7.8 (a) FTIR spectra of CO adsorbed on hydroxylated and pristine MgO(100)/Ag(100). Top trace: 0.02 ML gold on MgO (hydroxylated); second trace: 0.006 ML gold on pristine MgO; all following traces: 0.02 ML gold on pristine MgO. The spectra were collected at the indicated temperatures. The lower panel presents the results as an image plot with red being intense and blue representing no adsorption. (b) FTIR spectra of CO adsorbed on 0.02 ML Au/13 L MgO(001)/Ag(001) as a function of annealing temperature. The spectra were collected after recooling to 90 K and dosing with CO. (c) Model of the Au/MgO(001) surface representing the nature of gold species formed at various annealing temperature as deduced from the FTIR spectra in (b).

experimental and theoretical study has identified the species giving rise to a stretching frequency of 1850 cm^{-1} as CO adsorbed on single gold atoms [86]. The other component has been observed for gold clusters on various oxide supports and assigned to either very small gold clusters or partially positively charged gold sites at the cluster–oxide periphery (2121 cm^{-1}) [98, 99]. Frequencies in the range 2150–2180 cm^{-1} observed after deposition of 0.02 ML gold are typical for CO adsorbed on the cations of the MgO support [100]. However, according to Figure 7.7, positively charged gold species also give rise to CO stretching frequencies in this range. Since CO adsorption on MgO is weak, in general, a comparison of the thermal stability of adsorbed CO is a way to distinguish between adsorption on the substrate and on the gold particles, which is shown in Figure 7.8b. Additionally to presenting the data in a more graphical manner and including all annealing temperatures (too many to show in the top panel of Figure 7.8a), the same data are displayed in the lower panel of Figure 7.8a as an image plot. The signal according to CO on single gold atoms disappears at around 140 K, in agreement with a previous study [101]. The absorption band centered at 2121 cm^{-1} is stable to 220 K, whereas the two bands centered at 2170 and 2154 cm^{-1} merge into a single band at 2160 cm^{-1} by 120 K that is then stable to 240 K.

The experimental results shown in Figure 7.8a clearly indicate that the signals observed at 2154 and 2170 cm^{-1} are due to CO adsorption on gold particles on the MgO support. Both the frequency and the thermal stability of adsorbed CO are in line with the interpretation of these species as being due to CO adsorbed on positively charged gold species. It is interesting to note that the 2120 cm^{-1} state is lost at a similarly high temperature of 220 K, considerably higher than the typical CO desorption temperature from regular gold clusters on MgO (about 150 K) [102]. This is in line with the interpretation as CO adsorption sites in small gold clusters or cluster–oxide perimeter sites. Combining the results of Figure 7.8a leads to the conclusion that the initial nucleation of gold on the surface of the MgO(001) film at 90 K occurs at sites that give rise to positively charged gold species. These sites are occupied almost completely at the smallest gold coverage studied here. Therefore, their abundance is estimated to be below 0.5% ML. As the coverage is increased, single gold atoms (1850 cm^{-1}) and small gold clusters (2121 cm^{-1}) are stabilized on the surface, and finally large gold particles with bulk-like properties (2102 cm^{-1}) are formed.

The desorption temperature of 240 K observed for CO adsorbed on the positively charged gold species should be considered a lower bound because annealing is a dynamic process that affects the morphology of the gold particles initially formed at 90 K. In order to study the thermally induced agglomeration behavior of the gold particles, FTIR spectra were recorded following each annealing step after recooling the sample to 90 K and redosing CO. The result of this experiment is presented in Figure 7.8b, where the topmost spectrum represents the initial state of 0.02 ML gold after deposition at 90 K with four FTIR bands at 2170, 2154, 2121, and 1850 cm^{-1}. Up to an annealing temperature of 200 K the FTIR spectra in Figure 7.8a and b are almost identical, which indicates that the spectral changes can primarily be ascribed to morphological modifications due to enhanced diffusion and particle agglomeration. Single gold atoms are least stable on the surface and are lost at about 140 K. The sharp signal at 2121 cm^{-1} due to small gold particles becomes broad and shifts to lower wavenumber in the course of annealing to 200 K. We attribute this to thermally induced restructuring of the gold particles, which introduces heterogeneity in adsorption site distribution and CO adsorption geometry. Sintering and agglomeration proceed in the temperature range 200–300 K and lead to the disappearance of the positively charged gold species. Only a very weak CO signal at about 2110 cm^{-1} remains after annealing at 300 K (Figure 7.8b). Upon further annealing to 500 and 600 K a sharp and intense CO absorption signal is restored (2090 cm^{-1}). The weak FTIR absorption observed at 246 and 300 K in Figure 7.8b is ascribed to CO adsorption on gold particles with distinct morphology that are formed during annealing.

Figure 7.8c summarizes in a pictorial way the annealing-induced morphological changes of gold on the MgO surface. At low deposition temperature sharp CO absorption signals result from the presence of single gold atoms, small gold clusters, and particles nucleated at sites that give rise to positively charged gold. As the temperature is increased, enhanced diffusion leads to the formation of larger particles, which, at temperatures between 250 and 300 K, are flat and only two to three atomic layers high [103]. CO adsorption is only possible on the edge sites of these particles since the binding energy is too small for adsorption on the (111) top facet [104]. In addition, CO molecules adsorbed on the edge sites might be strongly tilted toward the surface, resulting in only weak FTIR absorption due to the metal surface selection rule. Only if the annealing temperature is increased above 300 K is the thermal energy sufficient for gold to form large, regular metallic nanoparticles that give rise to CO adsorption with the typical CO stretching frequency around 2100 cm^{-1}. It has to be noted that the apparent loss of CO FTIR signals at intermediate annealing temperatures is only observed for very small initial gold coverage. If this annealing experiment were to be performed with a sample with 0.2 ML gold, where large three-dimensional particles are present already after deposition at 90 K, the spectral changes in CO absorption signals would be much less pronounced [102].

The general conclusions drawn from FTIR spectra about nucleation and sintering of gold on MgO(001)/Ag(001) thin films are corroborated by corresponding X-ray photoemission studies, which are not discussed here in detail.

While the observed sintering behavior follows general expectations for the Au/MgO(001) system, the initial formation of positively charged gold species upon deposition of small quantities of gold, which results in rather high stretching frequencies of adsorbed CO, raises some questions about the nature of gold nucleation centers present on the surface of MgO thin films. Frequencies in the range 2130–2180 cm^{-1} are commonly observed for powder samples of oxide-supported gold clusters after oxidative treatment and have been assigned to CO adsorption on positively charged or oxidized gold particles [105]. At very small gold coverage, CO frequencies in this range have also been observed for model systems comprising gold on single-crystalline transition or rare earth metal oxide supports such as CeO_2 or Fe_3O_4 [106, 107]. While for those cases the positive charging of gold might be explained by the redox chemistry between the pristine support on the one hand and gold on the other [108], it is difficult to imagine such a mechanism being responsible for the formation of positively charged gold species on an MgO support. Instead, the interaction of gold with particular defects on the MgO surface seems to be more likely. At this point we note that slight differences in surface morphology and, hence, defectiveness of MgO films may influence the amount of hydroxyl groups on the MgO surface due to dissociation of residual water during the course of the experiment. Density functional calculations by Pacchioni and his group were performed for a variety of defects decorated with clusters containing a small number of gold atoms and adsorbed CO [109]. There are only two types of MgO defects that, when covered with small gold clusters containing a few gold atoms, and a CO molecule attached, would lead to CO stretching frequencies in the range 2154–2170 cm^{-1}. These bands arise from hydroxyls at edges and steps (2154 cm^{-1}) of an MgO(100) surface and F^{2+} centers, addressed in Section 7.2 (2170 cm^{-1}), decorated with Au_2 or Au_3 clusters. It turns out that the two decisive parameters controlling the formation of positively charged gold are the ionization potential of the Au_n species and the electron affinity of the electron trap (i.e., F^{2+} center and hydroxyl). The large ionization potential of gold atoms is lowered by several electron volts upon binding to the surface; however, this is only sufficient to allow for a charge transfer to the mentioned electron traps when very small clusters, that is, Au_n ($n = 2$–4), are considered. From an experimental point of view this requires an investigation of gold nucleation on hydroxylated MgO surfaces [110].

STM studies of a (deuteroxylated) hydroxylated MgO(100) surface, formed by exposing pristine MgO(100) to (heavy) water vapor at different pressures (10^{-6} and 1 mbar) which leads to 0.4 and 1 ML of hydroxyls, reveal morphological differences for gold deposits (Figure 7.9). A significant increase in gold particle density on hydroxylated MgO as compared to MgO(001) is observed: $4.2 \times 10^{12}\,\text{cm}^{-2}$ on hydroxylated MgO versus $2.8 \times 10^{12}\,\text{cm}^{-2}$ on MgO(001). In line with the increased particle density, the gold particle size is smaller on deuteroxylated MgO. Taking tip convolution effects into account, a mean diameter of 1.5 nm is estimated for gold particles on hydroxylated MgO, whereas it is 2.0 nm on MgO(001). It is safe to assume that nucleation and growth of gold on the nonhydroxylated MgO(001) surface proceed at particular surface sites, such as steps edges or point defects. Additional nucleation centers are created by surface hydroxylation. As evidenced by the FTIR spectral results only a particular type of deuteroxyl group (2737 cm^{-1}), which is associated with isolated OD groups formed by water dissociation at low-coordinated surface sites such as step edges, kinks, and corners, is able to chemically interact with incoming gold atoms.

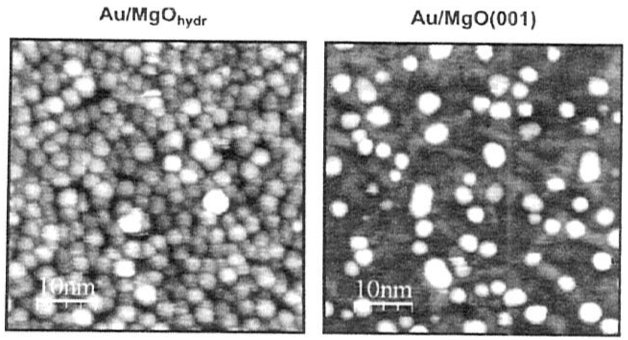

Figure 7.9 STM images of the same amount of gold deposited on hydroxylated and pristine MgO films [110].

In order to obtain more detailed insight into nucleation and sintering of gold on hydroxylated as compared to nonhydroxylated MgO surfaces, the evolution of gold-specific spectroscopic features following deposition at 100 K on MgO surfaces and after subsequent annealing steps up to 600 K was investigated using FTIR, with CO as a probe, and using X-ray photoelectron spectroscopy. Figure 7.8a shows one FTIR spectrum (out of many) taken following a 1 L exposure of CO at 100 K for 0.02 ML gold on 20 ML MgO_{hydr}. The spectrum was collected at 100 K. For MgO_{hydr} two broad features at 2166 and 2130 cm^{-1} are observed. These bands are blue-shifted and the intensity of the band at 2166 cm^{-1} is significantly different from the situation for the pristine film. After annealing to 600 K a single band remains at 2088 cm^{-1} similar to that of MgO(001). On MgO_{hydr} no contribution of CO adsorbed on gold atoms could be detected. The FTIR data indicate that the chemical state of gold after a final anneal to 600 K is the same on pristine and deutoroxylated MgO surfaces investigated here and corresponds to metallic gold particles. The scenario documented with FTIR is corroborated via X-ray photoelectron spectroscopy measurements where a strongly shifted gold component is observed concomitantly with the observation of the blue-shifted CO stretching frequency. This is a very strong indication that deuteroxyl groups present on the MgO(001) surface prior to gold deposition influence the nucleation, bonding, and electronic structure of gold on the MgO(001) surface in a wide temperature range. Very small gold clusters are reactive towards oxidation when deposited onto MgO_{hydr} whereas by contrast larger gold clusters are inert towards water vapor. The FTIR data provide clear evidence for a selectivity of the OD–gold interaction, which is found to affect only single coordinated (terminal) OD groups which have been detected in FTIR spectra taken in the range of OD vibrations (not shown). The stronger interaction of gold with a hydroxylated MgO surface due to the creation of strong Au—O interfacial bonds is responsible for the enhanced thermal stability and hence higher dispersion of gold clusters on MgO_{hydr} as compared to MgO(001). Considering that the catalytic literature has often favored the presence of positively charged gold as the active species in sharp contrast to most model studies where researchers have favored the presence of negatively charged gold, simply because positively charged gold was not detected (except the model studies described above), we must look into the reasons for this ambiguity.

To this end we look at the behavior of gold deposits on thin MgO(100) films on Mo(100) and the adsorption properties with respect to CO. Figure 7.10a shows an STM image of gold deposited on a thin MgO(100) film grown on Mo(100). The

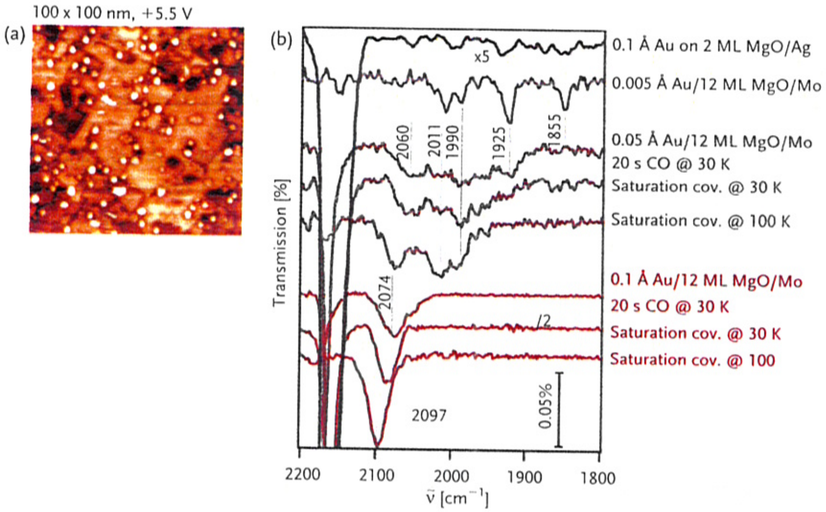

Figure 7.10 (a) STM topographic image of gold clusters deposited on a 12 ML thick, electron-bombarded MgO/Mo(001) film ($100 \times 100\,\text{nm}^2$, 5.5 V, 20 pA). The aggregates preferentially nucleate at the dislocation lines in the film. (b) Infrared absorption spectra [88].

gold deposits all reside on the grain boundaries of the film. We know from the discussion in Section 7.2 that those grain boundaries are loaded with electrons. Considering the rather high electron affinity of gold (within the Pauling scale gold is the metal with the largest electron affinity, close to that of the halogen iodine) we expect gold to charge negatively on such sites. Indeed, the FTIR spectra of adsorbed CO which are shown in Figure 7.10b for a number of different gold coverages and CO exposures indicate a wealth of different gold species, all with different CO stretching frequencies, but all are situated between $1850\,\text{cm}^{-1}$ (i.e., the monomer frequency discussed above) and the region typical for gold surfaces and rather large clusters. This region is typical for negatively charged gold. It has been shown earlier that the CO stretching frequency of Au^- depends strongly on the site of adsorption and cluster size. The data shown in the figure demonstrate that different gold clusters form on the surface, and many of them are negatively charged. This analysis is completely in line with vibrational spectra recorded for size-selected gold clusters in the gas phase reported by Gerard Meijer's group, who were able to compare CO stretching frequencies on gold clusters in the three different charge states of positive, neutral, and negative. It is also in line with reports of CO stretching frequencies for CO adsorbed on gold clusters, size selected in the gas phase, and then deposited onto an MgO(100) film on Mo(100). In the latter case Au_7 had been deposited and a stretching frequency of $2049\,\text{cm}^{-1}$ [82] had been observed, situated in the range of frequencies typical for negatively charged gold. However, the overarching conclusion drawn from those studies that this is due to gold residing on color center point defects that spontaneously form on MgO surfaces is incorrect. It is the specific system under investigation, that is, the MgO film on molybdenum, that is responsible. Since this model does not mimic the situation found in a powder, which may be used as a real catalyst, the conclusion that negatively charged gold is the active species in low-temperature CO oxidation is questionable. In fact, it is not unlikely that it might be positively charged gold. This example demonstrates that caution has to be exercised in characterizing the model system to properly describe the situation in the real system. Using only one experimental technique for characterization and using this in conjunction with theory is dangerous as documented in this example.

7.3.2
Oxides on Oxides: Vanadia Nanoparticles on Ceria

The next example is concerned with the reactivity of oxide nanoparticles supported by another oxide material. It is an established concept among catalyst scientists that so-called monolayer catalysts, where a reactive oxide, such as vanadia, is supported on a second oxide, such as ceria, exhibit considerably higher activity for methanol oxidation to formaldehyde. This does not mean that such catalysts may soon replace the iron molybdate-based catalysts currently used in industry, but it is interesting to try to understand the monolayer catalysts on a more detailed basis and to verify some of the ideas that have been put forward in the catalysis literature. The discussion is mainly based on results reviewed by Wachs [111], who compared vanadia overlayers on a number of support materials, such as SiO_2, Al_2O_3, ZrO_2, TiO_2, and CeO_2. Plotting the turnover for methanol oxidation to formaldehyde against the electronegativity of the support cations he noticed a nonlinear increase from SiO_2 to CeO_2 indicating that the support may play an active role in the process. In a combined experimental and theoretical effort together with Joachim Sauer's group, those systems have been studied using the described model catalyst approach [66, 105, 112–120]. Alumina, silica, and ceria have been studied as supports for vanadia deposits prepared by physical vapor deposition in oxygen ambient. Briefly, vanadia grows as three-dimensional clusters on both alumina and silica from low to high coverage. The vanadium is present in oxidation state (+3) in the volume of the clusters and in oxidation state (+5) at the surface as evidenced by photoelectron spectroscopy and the appearance of vanadyl vibrations which indicate the same surface termination of the clusters as found for $V_2O_3(0001)$ surfaces [66]. Those supported clusters oxidize methanol to formaldehyde at about 500 K, independent of vanadia coverage. On the basis of those studies it was possible to reassign the vibrational spectra of supported vanadia and identify vanadia–support interface vibrations that had been previously assigned to vanadyl vibrations of oligomeric vanadia deposits. While on silica and alumina three-dimensional growth of vanadia is observed, on ceria the predicted growth of monomeric, oligomeric, and two-dimensional (i.e., monolayer) vanadia is, in fact, observed and interesting correlations with spectroscopic data and reactivity may be drawn.

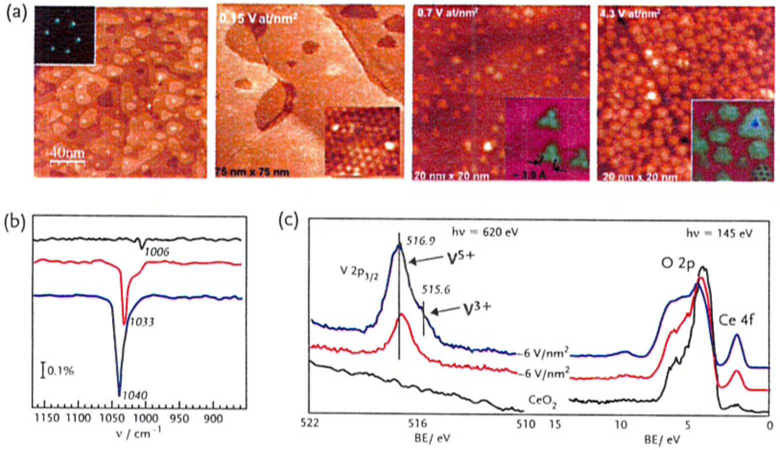

Figure 7.11 (a) STM images of $CeO_2(111)$ films on Ru(0001). Far left: clean; towards the right: increasing coverage of vanadium per nm^2 in oxygen as indicated. (b) FTIR spectra after vanadia deposition for three different coverages. (c) Photoelectron spectra before and after vanadia deposition on $CeO_2(111)$/Ru(0001) in the range of V $2p_{3/2}$ and the valence band ionization taken with synchrotron radiation at BESSY II [57].

Figure 7.11 shows a combination of STM images and vibrational and photoelectron spectra for vanadia deposits on ceria. The ceria support was grown as a thin film (thick enough to represent the bulk) [58] on an Ru(0001) single-crystal surface according to a procedure by Mullins *et al.* [59] and modified by the present author's group. STM images of the clean CeO_2 film are presented in Figure 7.6. Upon deposition of small amounts of vanadia, small, statistically distributed protrusions are observed which are accompanied by an infrared absoption spectrum indicative of isolated vanadyl groups. Upon increasing the coverage we see larger protrusions occurring (looking like trimers) which grow into two-dimensional islands with even a second layer on top of them. Parallel to this, a shift is observed of the vanadyl frequency to higher values compatible with dipolar coupling in the larger aggregates, and opposite to what was deduced from studies on powders. This is yet another example where model studies of well-defined structures can help to settle spectroscopic assignments. The infrared spectra are indicative of the formation of vanadyl (i.e., V(+5)) species which is corroborated by chemical shifts in X-ray photoelectron spectra (see Figure 7.11). The higher vanadia loadings show the occurrence of V(+3) species with the appearance of large aggregates in the STM images. It is interesting to note that parallel to this the valence band spectra show an increasing Ce(+3) signal near the Fermi energy. This can easily be explained by a redox mechanism upon vanadia adsorption. As the vanadia adopts its V(+5) oxidation state, it reduces the ceria in the film, originally in the Ce(+4) state to Ce(+3). Note that the small Ce(+3) signal in the clean film stems from Ce(+3) at defects (steps and vacancies).

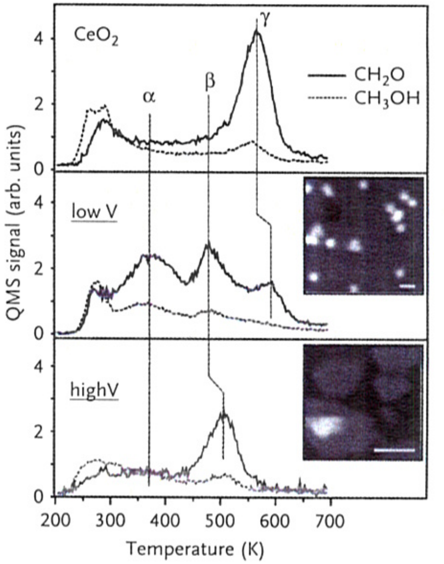

Figure 7.12 TPD spectra for approximately five layers of CH_3OH adsorbed at 300 K on $CeO_2(111)$ and $VO_x/CeO_2(111)$ surfaces at low (<2 V at nm^{-2}) and high (about 4 V at nm^{-2}) vanadia loadings. Solid lines indicate the raw signal for CH_2O (29 amu), whereas dashed lines indicate CH_3OH (31 amu, corrected for the methanol cracking pattern). Signal intensity below 300 K is assigned to the tail of CH_3OH monolayer desorption. (QMS, quadrupole mass spectrometer.) The insets show typical STM images of vanadia species at the respective coverage. The scale bar corresponds to 1 nm.

Such samples have been studied with respect to methanol oxidation to formaldehyde using temperature-programmed reaction (TPR). The outcome is interesting and is summarized in Figure 7.12 [119, 120]. While CeO_2 is active itself producing formaldehyde near 600 K, a higher loading of vanadia produces a TPR peak below or near 500 K similar to that of the larger clusters of vanadia on silica and alumina. For the monomers and small vanadia cluster species, which are not stable at high temperature, a TPR peak of considerably lower temperature (370 K) is observed. Hydrogen abstraction has been identified as the rate-limiting step in the oxidative dehydrogenation of propane and methanol [121, 122]. In the case of methanol, the hydrogen atom is abstracted from a surface-bound methoxy group. One of the electrons of the dissociated C—H bond forms a CH_2O surface radical, while the other one is transferred with the hydrogen atom to a surface oxygen site and results in a reduced metal ion. The Brønsted–Evans–Polanyi (BEP) principle suggests a linear relationship between energy barriers and reaction energies for catalytic steps which can be decomposed into C—H bond dissociation of surface methoxy and hydrogenation of oxygen species. When we consider different catalysts, the former is constant and, hence, the BEP principle suggests a linear relationship between the energy barriers and the hydrogenation energies of the surface oxygen species. With the hydrogenation energies of the following reaction:

$$VO_n/CeO_2(111) + 1/2H_2 \rightarrow VO_nH/CeO_2(111)$$

together with the oxygen defect creation energy, which is necessary to consider because a water molecule is formed from the hydrogenated vanadia species

$$VO_n/CeO_2(111) - 1/2O_2 \rightarrow VO_{n-1}/CeO_2(111)$$

we are in a position to construct a descriptor for methanol oxidation [121–124]. The more exoenergetic the hydrogenation the higher is the catalyst activity. It turns out through DFT calculations by Sauer and coworkers [120] that creating an oxygen vacancy on the vanadium-covered surface costs less energy than that on pristine ceria. Moreover, the electrons left on the surface are located on the ceria leaving vanadia in its highest oxidation state. The reducibility of the ceria does not diminish with the fraction of reduced ceria ions already present, because the electrons reside in 4f orbitals that do not interact with each other [61]. This fully supports the statement above and renders species such as monomers more reactive as is observed experimentally. In summary, this is another example where model studies may be employed to reveal detailed structure–reactivity relations, hardly possible for powder samples where structure may be deduced, at best, rather indirectly.

7.4
Ultrathin-Film Catalysts

We now move the discussion to the second class of system discussed in the introduction. Here we discuss ultrathin films where we have to consider interaction between the adsorbate on the thin film and the oxide–metal support interface [12]. We consider two examples: the first one is again dedicated to gold on MgO but this time MgO(100)/Ag(100); the second case study deals with the enhanced reactivity of a thin FeO layer on Pt(111). Some general remarks are appropriate at the outset.

In order to analyze the situation with the help of simple physical models, one has to consider, for example, the physical quantities that determine electron transfer from the metal substrate through the film [125]. These are, on the one hand, the ionization potential to excite an electron from the metal oxide, which is, in general, not simply the work function of the metal because it will be substantially modified by the presence of the oxide overlayer, and, on the other hand, the electron affinity of the species adsorbed on the oxide surface, which again may be influenced by the interaction with the oxide surfaces. If the energy balance between those quantities results in an energy gain, then electron transfer is possible, in principle. However, this is only part of a proper description, because it is not obvious how the quantity would depend on the thickness of the film, as the energy balance will only weakly depend on it for very thin films! Of course, in the case of films of several nanometers thickness, the tunneling probability would simply be zero. But why would an oxide film of three layers differ from one of eight layers with respect to tunneling? The reason is connected with the increased lattice flexibility of very thin films which is altered very rapidly as the film gets thicker, approaching quickly the phonon behavior of the bulk or a bulk-terminating surface. In other words, the thin film has the ability to accommodate the charge accumulated through electron transfer by a lattice distortion, a property which a thick film may not exhibit. This phenomenon is called a polaronic distortion and is well known from metal–semiconductor physics. One may use this knowledge to choose combinations of materials in thin oxide film design to produce systems with specific electronic properties with respect to electron transfer, which may in turn lead to specific chemical reactivity. Take, for example, cations, anions, or neutrals of one and the same species: They show different adsorption behavior and will undergo very different chemical reactions! Therefore, if we succeed in designing specific support systems which promote the formation of specific charge states, we might come to the point where we design catalysts for specific reactions. Of course, under reaction conditions one has to consider the presence of the gas phase as well, when we try to control the electron transfer by materials design because the gas phase determines the chemical potential of a catalyst. It is obvious that the phenomenon described, again, is a manifestation of the flexibility of the system, the unifying concept of this chapter.

As in Section 7.3, we will use gold metal nanoparticles as the object to study ultrathin-film phenomena. One open question concerns the state of charge of the gold particles in this case, an issue that, for thick films, we have addressed already in Section 7.3, showing how charging may be influenced by the presence of defects whose nature is dictated by the chosen model system. Another question refers to the site of reaction on the gold particles. One could imagine that all gold atoms of the particles show the same reactivity, or alternatively some specific sites could solely be responsible for the reactivity. For example, the gold atoms at the rim or circumference of the particle, which are in contact with the oxide substrate but are still accessible from the gas phase, could be candidates for such sites. To get closer to a solution, one can prepare samples with particles of varying sizes, starting from single gold atoms up to clusters containing 70 atoms or more, which is the size where the band gap closes and a transition to metallic gold in the classical sense occurs, on an MgO(100) film composed of three layers.

The oxide film is epitaxially grown on an Ag(001) surface, covering it completely, and its thickness is chosen such that electrons may be transferred from the MgO/Ag interface to the adsorbed gold particles in contrast to the situation in Section 7.3. We specifically have chosen Ag(100) over Mo(100) for this particular study because in the latter case, as discussed above, the electron trapping within grain boundaries determines the nucleation of metal, which we try to avoid here.

This charge transfer is reflected in the distribution of individual gold atoms on such an MgO(100) film as shown in Figure 7.13a [126, 127]. The gold atoms try to avoid close contact due to their negative charge leading to interatomic repulsion. If more gold is deposited a wetting of the surfaces occurs and a variety of

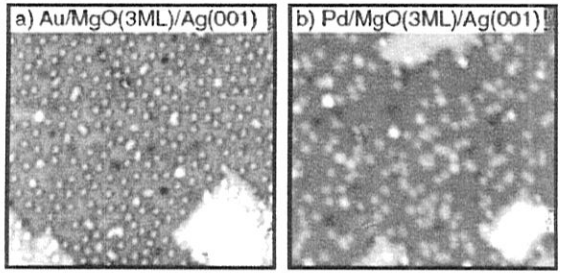

Figure 7.13 (a) STM image of gold deposited on 3 ML MgO on Ag(001). (b) STM image of palladium deposited on 3 ML MgO(001).

two-dimensional gold aggregates form, which are stable up to room temperature [103]. Had the experiments been performed on a thick MgO(100) film the objects would have grown into three-dimensional objects instead, as typically found for the growth of metals on oxides. Obviously, thin oxide films can be used as spacers to grow ideally flat metal–insulator structures at the smallest dimensions. It is necessary to point this out, and to remember that this statement strongly depends on the system. Had we deposited palladium instead of gold onto the thin MgO film (Figure 7.11b), we would have observed the growth of three-dimensional objects in the end, and neutral palladium atoms at the beginning, exhibiting a regular diffusion-limited spatial distribution [103]. Therefore, the general statement, often seen in the literature, that thin films should not be used as models for bulk oxide materials is very much misleading, as it is strongly dependent on the system studied.

As stated above, clusters of varying sizes were systematically studied. Au_1 to Au_7 clusters, which are mainly linear, and clusters with sizes between Au_{10} and Au_{20}, which are two-dimensional, have been imaged [128, 129]. Some examples have been studied in detail. In Figure 7.14 STM images of a flat Au_{18} cluster [130], obtained at a number of different voltages, are shown. Below the images differentiated current–voltage curves are plotted where the tip was placed at the positions indicated by dots in the images. The appearance of the images obviously depends markedly on the imaging voltage. This is a consequence of quantum mechanics that determines, of course, the electronic structure of the object. The unpaired 6s electrons of the gold atoms, constituting the cluster, lead to electron wave functions of the clusters that are strongly reminiscent of an electron gas confined to a two-dimensional potential well. The potential and the number of electrons determine the nodes in the electron density. The Au_{18} cluster, according to the schematic structure (shown in the central panel of Figure 7.14), is asymmetric. If one were to take away the one gold atom on the far right-hand side of the cluster one would create a symmetric Au_{17} cluster. We note in passing that, indeed, the stoichiometry of a given cluster may be established by using tip manipulation techniques [128, 129]. To understand the electronic structure we inspect the scanning tunneling spectra shown below the images in Figure 7.14. The maxima correspond to the electron distribution within cluster states represented by the conduction images shown above the spectra. One may recognize the position of the nodal planes in the spatial electron distributions. Also, the asymmetry induced by the eighteenth atom is clearly visible. Based on the position of the nodes it is also obvious why one does not observe all maxima in all scanning tunneling spectra: If the tip is positioned within a nodal plane there is no current to be detected for the specific state and consequently there is no maximum in the derivative. Tunneling spectra may be recorded for both occupied (negative voltages) and unoccupied (positive voltages) states. This allows one, in combination with model calculations and symmetry considerations, to "count" the number of electrons on the cluster [130, 131]. For Au_{18} a charge of four additional electrons is found. Therefore, the proper description of the system is (planar)/MgO(100).

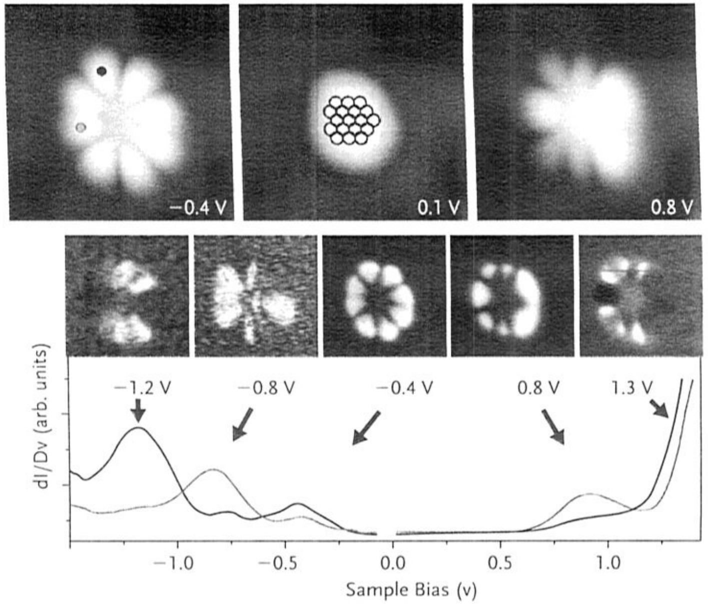

Figure 7.14 Set of images of Au_{18} at three different tunneling voltages and scanning tunneling spectra of Au_{18} from −2.0 eV to +2.0 eV recorded at two different positions as marked in the image taken at −0.4 eV. For the observed maxima and the conduction bond outset conduction images have been taken [130].

Next let us consider a larger gold island containing more than 100 gold atoms, conduction images of which are shown in Figure 7.15a [132]. Those images may well be simulated by calculations of two-dimensional gold islands containing edges and kinks. It turns out that the charge is mainly localized at the edge and preferentially at kinks of the island. Those are positions where acceptor molecules such as CO and O_2 will bind because the gold atoms are coordinatively unsaturated. Figure 7.15b shows experimental evidence for this: on the left, a topographic

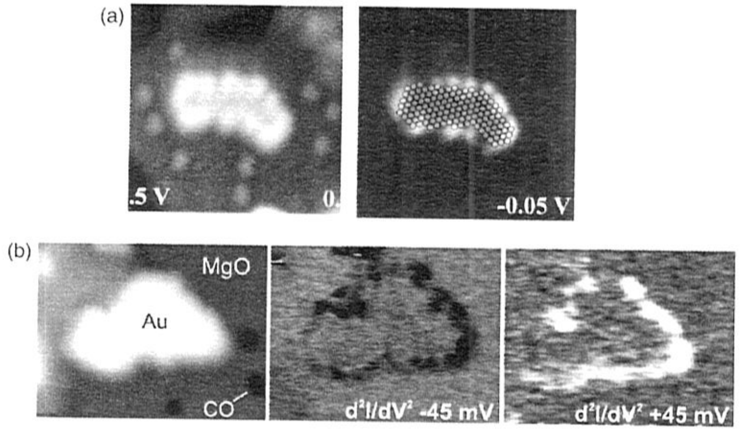

Figure 7.15 (a) STM images of gold islands on a 3 ML MgO(100) film before CO exposure as topographic image (left panel) and conductance image emphasizing the rim (right panel). A schematic of the island topography is overlaid. (b) STM image of a gold island on a trilayer MgO(100) film after exposure to CO (left panel). The two panels on the right show images taken at ±45 mV tunneling voltage using the second derivative. These are conditions to image tunneling losses (inelastic electron tunneling spectroscopy, IETS). The voltage corresponds to the hindered rotation of adsorbed CO. A prerequisite for meaningful IETS imaging is that one observes reversed contrast for opposite polarities [88].

STM image of a randomly chosen island that was exposed to CO is shown; in the center and on the right, the same island is imaged in a mode (second derivative) that allows for detection of inelastic losses in the tunneling current [88, 132]. In this particular case the characteristic frustrated rotation of adsorbed CO at 45 meV excitation energy has been probed and used for imaging. In the images one finds the vibration excited either by tunneling into (bright) or out of the sample (dark) only at the rim of the island, illustrating and identifying the preferential adsorption sites of CO molecules. One may therefore consider a scenario, when it comes to CO oxidation, where both molecules CO and O_2 bind to the cluster rim, and O_2 reacts either directly or after dissociation with co-adsorbed CO to CO_2.

A strong metal support interaction (SMSI) observed with particular catalyst systems, in which metal particles (such as palladium and platinum) strongly interact with a reducible support (such as titania), and are covered by a thin oxide film upon heating to elevated temperature [133], usually leads to reduced catalytic activity. The oxide film leads to a strong attenuation of adsorption capacity and, consequently, to a deactivation of the system. There have been many attempts to elucidate, even for model systems, the nature of the migrating oxide film. The best studied system is $Pt/TiO_2(110)$, but even in this case the attempts have been rather unsuccessful. Very recently, the present author and coworkers succeeded in preparing such a SMSI model system for which we were able to identify atomic structure of the encapsulated oxide film. The system is platinum supported on a $Fe_3O_4(111)$ film grown on a Pt(111) single crystal [134–137].

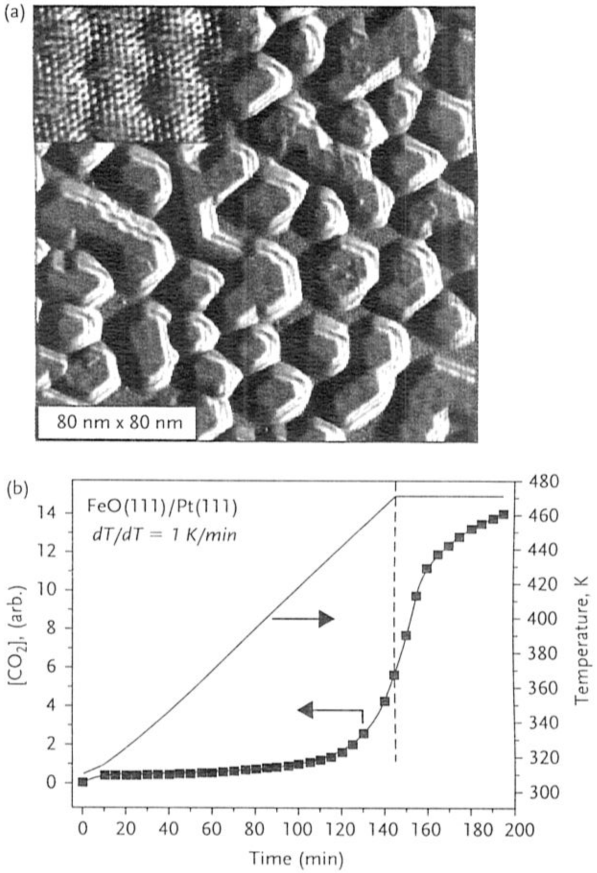

Figure 7.16 (a) STM image of platinum particles on $Fe_3O_4(111)$. The inset shows the atomic-resolution image taken on the top facet of one of the platinum particles. (b) CO oxidation on FeO(111)/Pt(111) as a function of time and temperatures ($1\ K\ min^{-1}$). The dotted line indicates the time when the temperature was held constant.

Figure 7.16a shows an STM image of this system after heating it to 850 K. After this treatment the CO adsorption capacity is drastically reduced which is typical of a SMSI effect. A close look at the STM images reveals well-structured and facetted nanoparticles. Moreover, atomically resolved images reveal corrugation that does not stem from platinum but rather from a well-ordered double-layer FeO(111) film, well described and characterized in the literature [29, 138–140]. As the oxide film covering platinum particles has been identified one may reduce the complexity of the model system by studying the properties of the bilayer FeO(111) film on a Pt(111) single crystal. Its structure has been studied in detail and characterized at the atomic level [29, 138–140]. The approximately 10% misfit between the FeO(111) lattice constant and that of Pt(111) gives rise to a typical

Moiré pattern in the STM image. This film is unreactive under ultrahigh vacuum conditions [141]. The situation changes dramatically, however, if one tests the system with respect to CO oxidation at ambient conditions (1 atm) in a reactor [141, 142] with careful control of the relative amounts of oxygen (one part, 20 mbar), CO (two parts, 40 mbar) and helium as buffer gas. If one ramps the temperature linearly at 1 K min^{-1} from 300 to 455 K, CO oxidation initiates at 430 K (Figure 7.16b).

An interesting observation is that this FeO/Pt(111) system at this temperature is by more than an order of magnitude more reactive than clean platinum. Usually, SMSI leads to an attenuated activity while here we observe a strong enhancement! Further studies as a function of different gas compositions, as well as thermal desorption studies, STM investigations, and detailed DFT model calculations reveal an interesting scenario that allows us to understand this phenomenon [137].

The scenario is depicted in Figure 7.17. The gas phase sets the chemical potential of the system. The steps shown are based on density functional calculations. Oxygen interacts with the double-layer FeO film on Pt(111) by pulling an iron atom up above the oxygen layer. This lowers the work function at the interface locally to allow for an electron transfer towards oxygen accompanied by the formation of a transient molecule which dissociates and results at higher oxygen coverage in the formation of a local O–Fe–O trilayer. There is, indeed, experimental evidence for the existence of such a trilayer. The central panel in Figure 7.17 shows an STM image of such a trilayer formed *in situ* at elevated O_2 pressure in a microscope [136, 137]. Its appearance is in particular determined by the Moiré structure of the FeO double layer and fills 80–90% of the surface as thermal desorption spectra indicate. The images are completely consistent with the structure suggested by the calculation, although the latter does not reproduce the patched morphology due to the enormous size of the unit cell, which was impossible to implement, but necessary to fully reproduce the details. Nevertheless, if the trilayer is exposed to CO the trilayer oxidizes the incoming CO to CO_2 via an Eley–Rideal mechanism leaving behind an oxygen vacancy in the film. At sufficiently high oxygen pressure the oxygen vacancy is filled again and the trilayer is sustained. If, however, the gas phase is oxygen poor the reaction finally stops because the trilayer is destroyed. Experimentally, we have confirmed [142] that the iron oxide film dewets the Pt(111) surface under CO-poor reaction conditions by forming small iron oxide particles, leaving Pt(111) surface open which then determines the reactivity of the systems opposite to a recent study in the literature [143]. Heating the dewetted surface in vacuum again leads to the formation of the FeO double layer, which then, at higher oxygen pressure, may be transformed into the trilayer again.

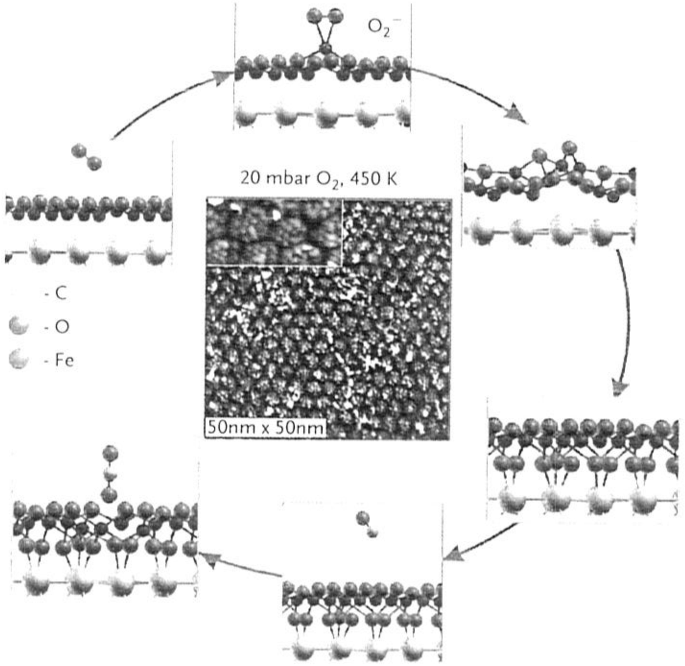

Figure 7.17 STM image of the active trilayer-FeO_{2-x} phase. The inset shows a high-resolution image [135]. The panels surrounding the image represent the individual steps in forming the active phase starting from FeO(111)/Pt(111), and its reaction with CO to form CO_2, as revealed by density functional calculations [136, 137].

Summarizing, we are in a position to understand the phenomena in the case of ultrathin oxide films on a similar basis as for the first examples of supported small metal clusters, as the electron transfer to oxygen is the key step to initiate the process. Superficially, we may come to the conclusion that we have identified a new concept to look at catalytic systems. Closer inspection reveals that this concept was used in the late 1940s by Cabrera and Mott [144] to understand metal oxidation and in the 1950s and 1960s by Vol'kenshtein to explain catalytic activity [145]. This concept was revived in the late 1980 is by Frost [146] and discussed by Boudart [147] and Ponec [148] subsequently. It has only been conceptually used, as noted by Haber [149], in electrocatalysis and in the discussions of the nonfaradaic electrochemical modification of catalytic activity effect by Vayenas and coworkers [150, 151] and not followed up, probably because tools to study systematically such systems at the atomic level were not applied. The time has come now!

7.5
Synopsis

Combined experimental and theoretical model studies are successful in disentangling structure–spectroscopy and structure–reactivity relationships as demonstrated for a few examples. Model systems may be characterized at the atomic level experimentally, which allows for direct comparison with theoretical modeling and allows useful correlations with systems of practical relevance. Thin oxide films on metal substrates represent an interesting and promising material combination. It is possible to use well-known concepts from semiconductor physics to understand the underlying principles and to use them to design model systems to get insight into elementary questions in catalysis. Maybe these new (old) concepts could be used as a guideline to design catalysts and also to understand systems that have been controversially discussed in the literature [152–155]. It is important to note that it is crucial to have appropriate experimental techniques at one's disposal to look at this. The design of a useful set of experimental techniques is a key goal of experimental research.

Acknowledgments

I would like to thank my coworkers and students and our guests at the department for their excellent work over almost three decades. Their names appear in the references and I am grateful to them for spending time in my laboratory and working with me. Many fruitful and illuminating discussions with partners in theory, Paul Bagus, Hannu Häkkinen, Gianfranco Pacchioni, and Joachim Sauer, are gratefully acknowledged. We thank the German Science Foundation through the Cluster of Excellence UniCat, the SFB 546 "Structure, Dynamics and Reactivity of Transition Metal Oxides," and the Fonds der Chemischen Industrie for support. I am delighted to have been part of an organization – the Max-Planck Society – that gave me the freedom to follow my ideas and dreams without many administrative constraints that other researchers have to endure.

References

1 Henrich, V.E. and Cox, P.A. (1994) *The Surface Science of Metal Oxides*, Cambridge University Press, Cambridge.

2 Charlton, G., Howes, P.B., Nicklin, C.L., Steadman, P., Taylor, J.S.G., Muryn, C.A., Harte, S.P., Mercer, J., McGrath, R., Norman, D., Turner, T.S., and Thornton, G. (1997) *Phys. Rev. Lett.*, **78**, 495.

3 Wu, M.-C. and Møller, P.J. (1989) *Surf. Sci.*, **224**, 250.

4 Chambers, S.A. (2000) *Surf. Sci. Rep.*, **39**, 105.

5 Goodman, D.W. (1995) *Surf. Rev. Lett.*, **2**, 9.

6 Freund, H.-J. (1995) *Ber. Bunsenges. Phys. Chem.*, **99**, 1261.

7 Freund, H.-J. (1997) *Angew. Chem. Int. Ed.*, **36**, 452.

8 Bäumer, M. and Freund, H.-J. (1999) *Prog. Surf. Sci.*, **61**, 127.

9 Freund, H.-J., Kuhlenbeck, H., and Staemmler, V. (1996) *Rep. Prog. Phys.*, **59**, 283.

10 Campbell, C.T. (1997) *Surf. Sci. Rep.*, **27**, 1.

11 Libuda, J. and Freund, H.-J. (2005) *Surf. Sci. Rep.*, **57**, 157.

12 Freund, H.-J. and Pacchioni, G. (2008) *Chem. Soc. Rev.*, **37**, 2224.

13 Nilius, N. (2009) *Surf. Sci. Rep.*, **64**, 595.

14 Freund, H.-J. (2007) *Surf. Sci.*, **601**, 1438.

15 Kuhlenbeck, H., Odörfer, G., Jaeger, R., Illing, G., Menges, M., Mull, T., Freund, H.-J., Pöhlchen, M., Staemmler, V., Witzel, S., Scharfschwerdt, C., Wennemann, K., Liedtke, T., and Neumann, M. (1991) *Phys. Rev. B*, **43**, 1969.

16 Freund, H.-J. and Goodman, D.W. (2008) in *Handbook of Heterogeneous Catalysis*, vol. **4**, 2nd edn (eds Ertl, G., Knözinger, H., Schüth, F., and Weitkamp, J.), Wiley-VCH Verlag GmbH, Weinheim, p. 1309.

17 Wu, M.C., Corneille, J.S., Estrada, C.A., He, J.-W., and Goodman, D.W. (1991) *Chem. Phys. Lett.*, **182**, 472.

18 He, J.-W., Estrada, C.A., Corneille, J.S., Wu, M.-C., and Goodman, D.W. (1992) *Surf. Sci.*, **261**, 164.

19 Wu, M.C., Estrada, C.A., and Goodman, D.W. (1991) *Phys. Rev. Lett.*, **67**, 2910.

20 Wu, M.-C., Estrada, C.A., Corneille, J.S., and Goodman, D.W. (1992) *J. Chem. Phys.*, **96**, 3892.

21 He, J.-W., Corneille, J.S., Estrada, C.A., Wu, M.C., and Goodman, D.W. (1992) *J. Vac. Sci. Technol. A*, **10**, 2248.

22 Wu, M.C. and Goodman, D.W. (1992) *Catal. Lett.*, **15**, 1.

23 Wu, M.C., Truong, C.M., Coulter, K., and Goodman, D.W. (1992) *J. Am. Chem. Soc.*, **114**, 7565.

24 Wu, M.C., Truong, C.M., and Goodman, D.W. (1992) *Phys. Rev. B*, **46**, 12688.

25 Wu, M.C., Truong, C.M., Coulter, K., and Goodman, D.W. (1993) *J. Vac. Sci. Technol. A*, **11**, 2174.

26 Corneille, J.S., He, J.-W., and Goodman, D.W. (1994) *Surf. Sci.*, **306**, 269.

27 Xu, X., Oh, W.S., and Goodman, D.W. (1996) *Langmuir*, **12**, 4877.

28 Jaeger, R.M., Kuhlenbeck, H., Freund, H.-J., Wuttig, M., Hoffmann, W., Franchy, R., and Ibach, H. (1991) *Surf. Sci.*, **259**, 235.

29 Vurens, G.H., Salmeron, M., and Somorjai, G.A. (1988) *Surf. Sci.*, **201**, 129.

30 Freund, H.-J. (2010) *Chem. Eur. J.*, **16**, 9384.

31 Benedetti, S., Benia, H.M., Nilius, N., Valeri, S., and Freund, H.J. (2006) *Chem. Phys. Lett.*, **430**, 330.

32 Trevethan, T. and Shluger, A. (2009) *Nanotechnology*, **20**, 264019.

33 Benia, H.M., Myrach, P., Nilius, N., and Freund, H.J. (2010) *Surf. Sci.*, **604**, 435.

34 Binnig, G., Frank, K.H., Fuchs, H., Garcia, N., Reihl, B., Rohrer, H., Salvan, F., and Williams, A.R. (1985) *Phys. Rev. Lett.*, **55**, 991.

35 Kolesnychenko, O.Y., Kolesnichenko, Y.A., Shklyarevskii, O.I., and van Kempen, H. (2000) *Physica B*, **291**, 246.

36 Freund, H.-J., Nilius, N., Risse, T., Schauermann, S., and Schmidt, T. (2011) *ChemPhysChem*, **12**, 79.

37 Benia, H.M., Nilius, N., and Freund, H.J. (2007) *Surf. Sci.*, **601**, L55.

38 Benia, H.M., Myrach, P., and Nilius, M. (2008) *New J. Phys.*, **10**, 013010.

39 Goniakowski, J. and Noguera, C. (2004) *Interface Sci.*, **12**, 93.

40 Giordano, L., Cinquini, F., and Pacchioni, G. (2006) *Phys. Rev. B*, **73**, 045414.

41 König, T., Simon, G.H., Rust, H.P., and Heyde, M. (2009) *J. Phys. Chem. C*, **113**, 11301.

42 McKenna, K.P. and Shluger, A.L. (2009) *Phys. Rev. B*, **79**, 224116.

43 Wollschläger, J., Erdös, D., and Schröder, K.M. (1998) *Surf. Sci.*, **402–404**, 272.

44 Wollschläger, J., Viernow, J., Tegenkamp, C., Erdös, D., Schröder, K.M., and Pfnür, H. (1999) *Appl. Surf. Sci.*, **142**, 129.

45 Valeri, S., Altieri, S., di Bona, A., Luches, P., Giovanardi, C., and Moia, T.S. (2002) *Surf. Sci.*, **507–510**, 311.

46 Giovanardi, C., di Bona, A., Moia, T.S., Valeri, S., Pisani, C., Sgroi, M., and Busso, M. (2002) *Surf. Sci.*, **505**, L209.

47 Schintke, S., Messerli, S., Pivetta, M., Patthey, F., Libioulle, L., Stengel, M., De Vita, A., and Schneider, W.-D. (2001) *Phys. Rev. Lett.*, **87**, 2768011.

48 Schintke, S. and Schneider, W.D. (2004) *J. Phys.: Condens. Matter*, **16**, R49.

49 Sterrer, M., Fischbach, E., Risse, T., and Freund, H.-J. (2005) *Phys. Rev. Lett.*, **94**, 186101.

50 Sterrer, M., Heyde, M., Novicki, M., Nilius, N., Risse, T., Rust, H.P.,

Pacchioni, G., and Freund, H.-J. (2006) *J. Phys. Chem. B*, **110**, 46.

51 Sterrer, M., Yulikov, M., Fischbach, E., Heyde, M., Rust, H.-P., Pacchioni, G., Risse, T., and Freund, H.J. (2006) *Angew. Chem. Int. Ed.*, **45**, 2630.

52 König, T., Simon, G.H., Martinez, U., Giordano, L., Pacchioni, G., Heyde, M., and Freund, H.-J. (2010) *ACS Nano*, **4**, 2510.

53 König, T., Simon, G.H., Rust, H.P., Pacchioni, G., Heyde, M., and Freund, H.J. (2009) *J. Am. Chem. Soc.*, **131**, 17544.

54 Shao, X., Myrach, P., Nilius, N., Freund, H.-J., Martinez Pozzoni, U., Prada, S., Giordano, L., and Pacchioni, G. (2011) *Phys. Rev. B*, in press.

55 Shao, X., Myrach, P., Nilius, N., and Freund, H.-J. (2011) *J. Phys. Chem. C*, **115**, 8784.

56 Ranke, W., Ritter, M., and Weiss, W. (1999) *Phys. Rev. B*, **60**, 1527.

57 M. Baron, H. Abbott, O. Bondarchuk, D. Stacchiola, A. Uhl, S. Shaikhutdinov, H.-J. Freund, C. Popa, Maria V. Ganduglia-Pirovano, J. Sauer, Angewandte Chemie International Edition 2009, 48, 8006.

58 Lu, J.L., Gao, H.J., Shaikhutdinov, S., and Freund, H.J. (2006) *Surf. Sci.*, **600**, 5004.

59 Mullins, D.R., Radulovic, P.V., and Overbury, S.H. (1999) *Surf. Sci.*, **429**, 186.

60 Jerratsch, J.F., Shao, X., Nilius, N., Freund, H.-J., Popa, C., Ganduglia-Pirovano, M.V., Burow, A.M., and Sauer, J. (2011) *Phys. Rev. Lett.*, **106**, 246801.

61 Ganduglia-Pirovano, M.V., Da Silva, J. L.F., and Sauer, J. (2009) *Phys. Rev. Lett.*, **102**, 026101.

62 Xu, C., Hassel, M., Kuhlenbeck, H., and Freund, H.-J. (1991) *Surf. Sci.*, **258**, 23.

63 Shaikhutdinov, S.K. and Weiss, W. (1999) *Surf. Sci.*, **432**, L627.

64 Lemire, C., Bertarione, S., Zecchina, A., Scarano, D., Chaka, A., Shaikhutdinov, S., and Freund, H.J. (2005) *Phys. Rev. Lett.*, **94**, 166101.

65 Dupuis, A.-C., Abu Haija, M., Richter, B., Kuhlenbeck, H., and Freund, H.J. (2003) *Surf. Sci.*, **539**, 99.

66 Göbke, D., Romanyshyn, Y., Guimond, S., Sturm, J.M., Kuhlenbeck, H., Döbler, J., Reinhardt, U., Ganduglia-Pirovano, M.V., Sauer, J., and Freund, H.J. (2009) *Angew. Chem. Int. Ed.*, **48**, 3695.

67 Weiss, W. and Ranke, W. (2002) *Prog. Surf. Sci.*, **70**, 1.

68 Shaikhutdinov, S., Ritter, M., Wang, X.-G., Over, H., and Weiss, W. (1999) *Phys. Rev. B*, **60**, 11062.

69 Schmal, M. and Freund, H.-J. (2009) *An. Acad. Bras. Cienc.*, **81**, 297.

70 Haruta, M. (2002) *CatTech*, **6**, 102.

71 Bond, G.C. and Thompson, D.T. (2000) *Gold Bull.*, **33**, 41.

72 Fierro-Gonzalez, J.C. and Gates, B.C. (2007) *Catal. Today*, **122**, 201.

73 Kung, M.C., Davis, R.J., and Kung, H. H. (2007) *J. Phys. Chem. C*, **111**, 11767.

74 Janssens, T.V.W., Clausen, B.S., Hvolbæk, B., Falsig, H., Christensen, C.H., Bligaard, T., and Nørskov, J.K. (2007) *Top. Catal.*, **44**, 15.

75 Chrétien, S., Buratto, S.K., and Metiu, H. (2007) *Curr. Opin. Solid State Mater. Sci.*, **11**, 62.

76 Coquet, R., Howard, K.L., and Willock, D.J. (2008) *Chem. Soc. Rev.*, **37**, 2046.

77 Frank, M., Bäumer, M., Kühnemuth, R., and Freund, H.-J. (2001) *J. Phys. Chem. B*, **105**, 8569.

78 Meyer, R., Lemire, C., Shaikhutdinov, S., and Freund, H.-J. (2004) *Gold Bull.*, **37**, 72.

79 Bond, G.C. and Thompson, D.T. (1999) *Catal. Rev. Sci. Eng.*, **41**, 319.

80 Mihaylov, M., Knözinger, H., Hadjiivanov, K., and Gates, B.C. (2007) *Chem. Ing. Tech.*, **79**, 795.

81 Sterrer, M., Yulikov, M., Fischbach, E., Heyde, M., Rust, H.-P., Pacchioni, G., Risse, T., and Freund, H.-J. (2006) *Angew. Chem. Int. Ed.*, **45**, 2630.

82 Yoon, B., Häkkinen, H., Landman, U., Wörz, A., Antonietti, J.-M., Abbet, S., Judai, K., and Heiz, U. (2005) *Science*, **307**, 403.

83 Fielicke, A., von Helden, G., Meijer, G., Simard, B., and Rayner, D.M. (2005) *J. Phys. Chem. B*, **109**, 23935.

84 Blyholder, G. (1964) *J. Phys. Chem.*, **68**, 2772.

85 Bagus, P. and Pacchioni, G. (2008) *J. Phys.: Conf. Ser.*, **117** 012003.

86 Sterrer, M., Yulikov, M., Risse, T., Freund, H.J., Carrasco, J., Illas, F., Di Valentin, C., Giordano, L., and Pacchioni, G. (2006) *Angew. Chem. Int. Ed.*, **45**, 2633.

87 Giordano, L., Carrasco, J., Di Valentin, C., Illas, F., and Pacchioni, G. (2006) *J. Chem. Phys.*, **124**, 174709.

88 Lin, X., Yang, B., Benia, H.M., Myrach, P., Yulikov, M., Aumer, A., Brown, M., Sterrer, M., Bondarchuk, O., Kieseritzky, E., Rocker, J., Risse, T., Gao, H., Nilius, N., and Freund, H.J. (2010) *J. Am. Chem. Soc.*, **132**, 7745.

89 Libuda, J., Frank, M., Sandell, A., Andersson, S., Brühwiler, P.A., Bäumer, M., Mårtensson, N., and Freund, H.-J. (1997) *Surf. Sci.*, **384**, 106.

90 Starr, D.E., Diaz, S.F., Musgrove, J.E., Ranney, J.T., Bald, D.J., Nelen, L., Ihm, H., and Campbell, C.T. (2002) *Surf. Sci.*, **515**, 13.

91 Jensen, M.C.R., Venkataramani, K., Helveg, S., Clausen, B.S., Reichling, M., Besenbacher, F., and Lauritsen, J. V. (2008) *J. Phys. Chem. C*, **112**, 16953.

92 Chambers, S.A., Droubay, T., Jennison, D.R., and Mattsson, T.R. (2002) *Science*, **297**, 827.

93 Fu, Q., Wagner, T., and Rühle, M. (2006) *Surf. Sci.*, **600**, 4870.

94 Niu, C., Shepherd, K., Martini, D., Tong, J., Kelber, J.A., Jennison, D.R., and Bogicevic, A. (2000) *Surf. Sci.*, **465**, 163.

95 Lazzari, R. and Jupille, J. (2005) *Phys. Rev. B*, **71**, 045409.

96 Moreau, F., Bond, G.C., and Taylor, A. O. (2005) *J. Catal.*, **231**, 105.

97 Qian, K., Fang, J., Huang, W., He, B., Jiang, Z., Ma, Y., and Wei, S. (2010) *J. Mol. Catal. A*, **320**, 97.

98 Lemire, C., Meyer, R., Shaikhutdinov, S.K., and Freund, H.J. (2004) *Surf. Sci.*, **552**, 27.

99 Boronat, M., Concepcioón, P., and Corma, A. (2009) *J. Phys. Chem. C*, **113**, 16772.

100 Sterrer, M., Risse, T., and Freund, H.-J. (2005) *Surf. Sci.*, **596**, 222.

101 Yulikov, M., Sterrer, M., Risse, T., and Freund, H.J. (2009) *Surf. Sci.*, **603**, 1622.

102 Brown, M.A., Carrasco, E., Sterrer, M., and Freund, H.-J. (2010) *J. Am. Chem. Soc.*, **132**, 4064.

103 Sterrer, M., Risse, T., Heyde, M., Rust, H.-P., and Freund, H.-J. (2007) *Phys. Rev. Lett.*, **98**, 206103.

104 Sicolo, S., Giordano, L., and Pacchioni, G. (2009) *J. Phys. Chem. C*, **113**, 10256.

105 Baron, M., Bondarchuk, O., Stacchiola, D., Shaikhutdinov, S., and Freund, H.J. (2009) *J. Phys. Chem. C*, **113**, 6042.

106 Wu, Z., Zhou, S., Zhu, H., Dai, S., and Overbury, S.H. (2009) *J. Phys. Chem. C*, **113**, 3726.

107 Naya, K., Ishikawa, R., and Fukui, K.-i. (2009) *J. Phys. Chem. C*, **113**, 10726.

108 Rim, K.T., Eom, D., Liu, L., Stolyarova, E., Raitano, J.M., Chan, S.-W., Flytzani-Stephanopoulos, M., and Flynn, G.W. (2009) *J. Phys. Chem. C*, **113**, 10198.

109 Brown, M., Ringleb, F., Fujimori, Y., Sterrer, M., Freund, H.-J., Preda, G., and Pacchioni, G. (2011) *J. Phys. Chem. C*, **115**, 10114.

110 Brown, M., Fujimori, Y., Ringleb, F., Shao, X., Stavale, F., Nilius, N., Sterrer, M., and Freund, H.-J. (2011) *J. Am. Chem. Soc.*, in press.

111 Wachs, I.E. (2005) *Catal. Today*, **100**, 79.

112 Magg, N., Giorgi, J.B., Schroeder, T., Bäumer, M., and Freund, H.J. (2002) *J. Phys. Chem. B*, **106**, 8756.

113 Magg, N., Immaraporn, B., Giorgi, J., Schroeder, T., Bäumer, M., Döbler, J., Wu, Z., Kondratenko, E., Cherian, M., Baerns, M., Stair, P.C., Sauer, J., and Freund, H.-J. (2004) *J. Catal.*, **226**, 88.

114 Guimond, S., Abu Haija, M., Kaya, S., Lu, J., Weissenrieder, J., Shaikhutdinov, S., Kuhlenbeck, H., Freund, H.-J., Döbler, J., and Sauer, J. (2006) *Top. Catal.*, **38**, 117.

115 Kaya, S., Sun, Y.N., Weissenrieder, J., Stacchiola, D., Shaikhutdinov, S., and Freund, H.J. (2007) *J. Phys. Chem. C*, **111**, 5337.

116 Guimond, S., Sturm, J.M., Göbke, D., Romanyshyn, Y., Naschitzki, M., Kuhlenbeck, H., and Freund, H.-J. (2008) *J. Phys. Chem. C*, **112**, 11835.

117 Romanyshyn, Y., Guimond, S., Kuhlenbeck, H., Kaya, S., Blum, R.P., Niehus, H., Shaikhutdinov, S., Simic-Milosevic, M., Nilius, N., Freund, H.J., Ganduglia-Pirovano, M.V., Fortrie, R., Döbler, J., and Sauer, J. (2008) *Top. Catal.*, **50**, 106.

118 Sturm, J.M., Göbke, D., Kuhlenbeck, H., Döbler, J., Reinhardt, U., Ganduglia-Pirovano, M.V., Sauer, J., and Freund, H.J. (2009) *Phys. Chem. Chem. Phys.*, **11**, 3290.

119 Abbott, H.L., Uhl, A., Baron, M., Lei, Y., Meyer, R.J., Stacchiola, D.J., Bondarchuk, O., Shaikhutdinov, S., and Freund, H.J. (2010) *J. Catal.*, **272**, 82.

120 Ganduglia-Pirovano, M.V., Popa, C., Sauer, J., Abbott, H., Uhl, A., Baron, M., Stacchiola, D., Bondarchuk, O., Shaikhutdinov, S., and Freund, H.-J. (2010) *J. Am. Chem. Soc.*, **132**, 2345.

121 Döbler, J., Pritzsche, M., and Sauer, J. (2005) *J. Am. Chem. Soc.*, **127**, 10861.

122 Rozanska, X., Fortrie, R., and Sauer, J. (2007) *J. Phys. Chem. C*, **111**, 6041.

123 Sauer, J. and Döbler, J. (2004) *Dalton Trans.*, 3116.

124 Kim, H.Y., Lee, H.M., Pala, R.G.S., Shapovalov, V., and Metiu, H. (2008) *J. Phys. Chem. C*, **112**, 12398.

125 Giordano, L., Martinez, U., Sicolo, S., and Pacchioni, G. (2007) *J. Chem. Phys.*, **127**, 144713.

126 Sterrer, M., Risse, T., Giordano, L., Heyde, M., Nilius, N., Rust, H.P., Pacchioni, G., and Freund, H.-J. (2007) *Angew. Chem. Int. Ed.*, **46**, 8703.

127 Sterrer, M., Risse, T., Martinez Pozzoni, U., Giordano, L., Heyde, M., Rust, H.-P., Pacchioni, G., and Freund, H.-J. (2007) *Phys. Rev. Lett.*, **98**, 096107.

128 Simic-Milosevic, V., Heyde, M., Nilius, N., Koenig, T., Rust, H.P., Sterrer, M., Risse, T., Freund, H.J., Giordano, L., and Pacchioni, G. (2008) *J. Am. Chem. Soc.*, **130**, 7814.

129 Simic-Milosevic, V., Heyde, M., Lin, X., König, T., Rust, H.-P., Sterrer, M., Risse, T., Nilius, N., Freund, H.-J., Giordano, L., and Pacchioni, G. (2008) *Phys. Rev. B*, **78**, 235429.

130 Lin, X., Nilius, N., Freund, H.J., Walter, M., Frondelius, P., Honkala, K., and Häkkinen, H. (2009) *Phys. Rev. Lett.*, **102**, 206801.

131 Nilius, N., Ganduglia-Pirovano, M.V., Brázdová, V., Kulawik, M., Sauer, J., and Freund, H.J. (2008) *Phys. Rev. Lett.*, **100**, 096802.

132 Lin, X., Nilius, N., Sterrer, M., Koskinen, P., Häkkinen, H., and Freund, H.-J. (2010) *Phys. Rev. B*, **81**, 153406.

133 Van Delft, F.C.M.J.M. and Nieuwenhuys, B.E. (1985) *Solid State Ionics*, **16**, 233.

134 Qin, Z.H., Lewandowski, M., Sun, Y. N., Shaikhutdinov, S., and Freund, H.J. (2008) *J. Phys. Chem. C*, **112**, 10209.

135 Qin, Z.H., Lewandowski, M., Sun, Y. N., Shaikhutdinov, S., and Freund, H.J. (2009) *J. Phys.: Condens. Matter*, **21**, 134019.

136 Lewandowski, M. (2010) PhD thesis, Technical University (Berlin).

137 Sun, Y.-N., Giordano, L., Goniakowski, J., Lewandowski, M., Qin, Z.-H., Noguera, C., Shaikhutdinov, S., Pacchioni, G., and Freund, H.-J. (2010) *Angew. Chem. Int. Ed.*, **49**, 4418.

138 Galloway, H.C., Benitez, J.J., and Salmeron, M. (1993) *Surf. Sci.*, **298**, 127.

139 Weiss, W., Barbieri, A., Van Hove, M.A., and Somorjai, G.A. (1848) *Phys. Rev. Lett.*, **1993**, 71.

140 Vurens, G.H., Maurice, V., Salmeron, M., and Somorjai, G.A. (1992) *Surf. Sci.*, **268**, 170.

141 Sun, Y.N., Qin, Z.H., Lewandowski, M., Carrasco, E., Sterrer, M., Shaikhutdinov, S., and Freund, H.J. (2009) *J. Catal.*, **266**, 359.

142 Sun, Y.N., Qin, Z.H., Lewandowski, M., Kaya, S., Shaikhutdinov, S., and Freund, H.J. (2008) *Catal. Lett.*, **126**, 31.

143 Fu, Q., Li, W.-X., Yao, Y., Hongyang, L., Fu, Q., Su, H.-Y., Ma, D., Gu, X.-K., Chen, L., Wang, Z., Zhang, H., Wang, B., and Bao, X. (2010) *Science*, **328**, 1141.

144 Cabrera, N. and Mott, N.F. (1948) *Rep. Prog. Phys.*, **12**, 163.

145 Vol'kenshtein, F.F. (1966) *Russ. Chem. Rev.*, **35**, 537.

146 Frost, J.C. (1988) *Nature*, **334**, 577.

147 Boudart, M. (1992) *Catal. Lett.*, **13**, 153.

148 Ponec, V. (1991) *Catal. Lett.*, **11**, 249.

149 Grzybowska-Swierkosz, B. and Haber, J. (1994) *Annu. Rep. Prog. Chem. C: Phys. Chem.*, **91**, 395.

150 Vayenas, C.G. and Koutsodontis, C.G. (2008) *J. Chem. Phys.*, **128**, 182506.

151 Tsampas, M.N., Sapountzi, F.M., and Vayenas, C.G. (2009) *Catal. Today*, **146**, 351.

152 Peden, C.H.F. and Goodman, D.W. (1986) *J. Phys. Chem.*, **90**, 1360.

153 Over, H. and Muhler, M. (2003) *Prog. Surf. Sci.*, **72**, 3.

154 Reuter, K., Stampfl, C., Ganduglia-Pirovano, V., and Scheffler, M. (2002) *Chem. Phys. Lett.*, **352**, 311.

155 Rosenthal, D., Girgsdies, F., Timpe, O., Blume, R., Weinberg, G., Teschner, D., and Schlögl, R. (2009) *Z. Phys. Chem.*, **233**, 183.